ASTRONOMICAL INSTITUTE
SLOVAK ACADEMY OF SCIENCES

CONTRIBUTIONS OF THE ASTRONOMICAL OBSERVATORY SKALNATÉ PLESO

• VOLUME LV •

Number 1

February 2025

ISSN: 1336–0337 (on-line version)

CODEN: CAOPF8

Editorial Office: Astronomical Institute of the Slovak Academy of Sciences
SK - 059 60 Tatranská Lomnica, The Slovak Republic

CONTENTS

EDITORIAL

INSTRUMENTS

STARS

The Contributions of the Astronomical Observatory Skalnaté Pleso
are available in the full version
in the frame of ADS Abstract Service
and can be downloaded in a usual way from the URL address:

https://ui.adsabs.harvard.edu/

as well as from the website of
the Astronomical Institute of the Slovak Academy of Sciences
on the URL address:

https://www.astro.sk/caosp/caosp.php

The journal is covered/indexed by:

Web of Science (WoS)
WoS Core Collection: Science Citation Index Expanded

SCOPUS

Index Copernicus International

EDITORIAL

In the 54-th edition of the journal Contributions of the Astronomical Observatory Skalnaté Pleso (CAOSP), 11 regular articles on 228 pages in three issues and 32 articles on 242 pages in the form of one "Special Issue" were published in 2024. According to the *Journal Citation Reports* database, the articles published in 2023 received 167 citations corresponding to the journal impact factor (JIF) of 0.4 and the JIF Quartile Q4.

Volume 54/1 published four regular articles. Two papers presented a useful software: (i) Mapping the main-belt asteroid's passages through known meteoroid streams, and (ii) performing the internal consistency between mean geocentric parameters and mean elements of a meteor shower. One article was devoted to the dwarf nova V503 Cyg, focused on the analysis of its super-outburst, a normal outburst, and a quiescent phase, mostly based on the TESS data. One purely theoretical article dealt with modeling a normal stars structure within the generalized polytropic model.

Volume 54/2 introduces selected contributions based on lectures from proceedings of our workshop "Observing techniques, instrumentation and science for metre-class telescopes III", held in Tatranská Lomnica during September 11.-15., 2023. The conference was organized on the occasion of the 80th anniversary of the first observations at the Skalnaté Pleso Observatory. The main goal of the conference was to highlight the significant role of small telescopes in astronomy and astrophysics research. The conference showed the importance of small telescopes in carrying out long-term monitoring programs, high-cadence observations of transient phenomena and all-sky surveys by robotic telescopes.

Volume 54/3 published three extended papers. The first deals with the light curve analysis for the two eclipsing binary stars EM Cet and EL Cen, while the second one presents an investigation of a pair of open clusters NGC 7031 and NGC 7086 utilizing Gaia DR3. The third theoretical article considers an interesting property of gravity within the general relativity that causes the innermost parts of ultra-compact objects (e.g. neutron stars) to be hollow.

Volume 54/4 published four regular articles. The first one presents an interesting method that allows us to characterize and detect classical Be and Herbig Ae/Be stars in Gaia low-resolution BP/RP spectra, which can distinguish emission-line objects from normal stars. Another interesting article presents photometric measurements of asteroid (12499) 1998 FR47, in which the authors investigate its rotational properties and the possibility of being a binary system. There is also one theoretical article presenting modeling of the internal structure of hot white dwarfs within a hybrid model. Finally, standard modeling of the light curves of W UMa type binaries can also be found.

To make the published manuscripts more "reader-friendly" we made some minor changes in our LaTeX and bibTeX styles (version 3.10). The hypertext links for references with DOI are now available in the resulting PDF.

Tatranská Lomnica, January, 2025

Augustín Skopal, Editor-in-Chief

Richard Komžík, Managing Editor

Contrib. Astron. Obs. Skalnaté Pleso **55/1**, 7 – 17, (2025)
https://doi.org/10.31577/caosp.2025.55.1.7

The new 50-cm multi-purpose telescope of the Russian-Cuban observatory

M. Ibrahimov[1], M. Sachkov[1], M. Nalivkin[1], S. Naroenkov[1], A. Shugarov[1], O. Pons Rodriguez[2], Z. Barcena Fonseca[2] and V. Shmagin[1]

[1] *Institute of Astronomy of the Russian Academy of Sciences, 48 Pyatnitskaya str. 119017, Moscow, Russia (E-mail: mansur@inasan.ru)*

[2] *Institute of Geophysics and Astronomy, Calle 212 No. 2906, 11 600, Havana, Cuba*

Received: November 4, 2024; Accepted: November 18, 2024

Abstract. Since 2017 the Institute of Astronomy of the Russian Academy of Sciences (Russia) and Institute of Geophysics and Astronomy (Cuba) have been implementing a joint international project with the aim of building a distributed global optical telescope network. The first 20 cm aperture robotic telescope of the the Russian-Cuban network has been operating since 2021 in Havana. It has a 3.5×3.5 degree field of view and a FLI PL16803 4K CCD camera with a set of UBVRI photometric filters. Construction of the second 50 cm telescope near Kislovodsk (Russia) has been underway since 2023 and it will be finished at the end of 2024, its scientific operation will start in early 2025. By 2030, the plan is to build the third 1 m telescope at Valle de Picadura (Cuba). The main parameters and scientific equipment of the new 50 cm telescope are described and its role in the Russian-Cuban distributed global telescope network is discussed.

Key words: telescopes – wide field telescopes – astronomical observations

1. Introduction

Since 2017 the Institute of Astronomy of the Russian Academy of Sciences (INASAN, Russia) and Institute of Geophysics and Astronomy (IGA, Cuba) have been developing a joint international project with the aim of building a distributed multi-task network of optical telescopes RCO (Russian-Cuban Observatory) (Bisikalo et al. (2018)).

At the beginning of 2021, the first telescope was installed at IGA in Havana (Bisikalo et al. (2022)). In 2023, the second optical telescope of a 50 cm aperture began being built in Russia.

According to the current plan, the third custom 1 m wide-field telescope based on INASAN's experience to build a 1 m modern telescope with a 9k detector (Ibrahimov et al. (2020); Shugarov et al. (2020); Ibrahimov (2019)) having spectroscopic, astrometric and photometric capabilities will be installed in 2030 at Villa de Picadura located 80 km east of Havana.

2. RCO network

The time difference of 8 hours (120 degrees) between Cuba and Russia (Kislovodsk) allows for continuous observations of up to 16 hours, which makes the RCO an efficient tool for many observational tasks requiring a long continuous observation series of the studied objects (see Fig. 1). The location of the second telescope in Russia significantly boosts the functionality of the Russian-Cuban network both in terms of global coverage and observation modes.

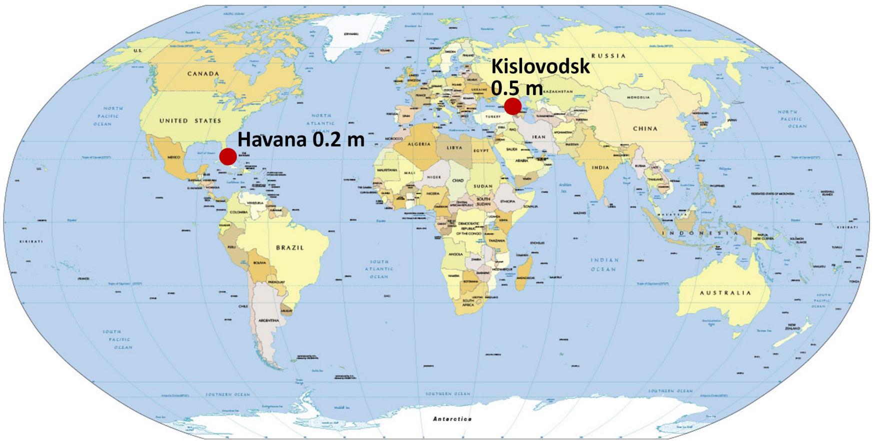

Figure 1. Russian-Cuban network of optical telescopes (RCO).

Among scientific goals, we can reference the detection and tracking of newly discovered asteroids (Ibrahimov et al. (2021)), photometric studies of variable stars (Savanov et al. (2024, 2023); Naroenkov et al. (2022a,b)) and the study of optical transient events, e.g. sources of gamma-ray bursts and tidal disruption events.

At least two types of telescopes should be included in the network – wide-field survey telescopes and middle-aperture follow-up telescopes equipped with cameras and spectrographs.

The first telescope of the Russian-Cuban network is a multipurpose photometric robotic telescope, which has a 20 cm aperture, 3 degree field of view and a set of UBVRI filters. The most interesting new objects, discovered by the 20 cm wide field telescope, will be studied in more detail with larger telescopes both in spectroscopic and photometric modes.

For this purpose, in the frame of the stage 2 of the RCO network development, the second 50 cm telescope with two main scientific instruments for spectroscopy and photometry is under construction.

For the second RCO observation station, the Kislovodsk observatory in the North Caucasus at the altitude of 2070 m was chosen. The observatory already has all key infrastructure and is easily accessible from the closest city of Kislovodsk.

This site has relatively good astronomical seeing for the central part of Russia. According to (Kornilov et al. (2016a)), the median moonless night-sky brightness is 22.1, 21.1, 20.3 and 19.0 mag per square arcsec for the B, V, R and I spectral bands, respectively. The annual amount of clear night astronomical time is, on average, 1320 h, i.e. 45% of the possible amount at the latitude of the observatory (Kornilov et al. (2016b)).

3. 50 cm telescope for the second RCO station

The second RCO observation station close to Kislovodsk will be equipped with:

– Astrosib RC500 0.5 m aperture telescope;

– custom-made focal unit with a switchable diagonal mirror for fast (about 15 s) switching between two scientific instruments;

– FLI Kepler 4040 FSI camera with Johnson-Cousins-Bessel UBVRI filters;

– suspended BACHES spectrograph with a ZWO ASI294 MM camera and active optics;

– ASA DDM100 direct drive mount;

– Astrosib ASD-4.5 dome.

The new 50 cm telescope RC500 for the second RCO observation station is produced by ASTROSIB Ltd, Russia (see Fig. 2). It has a 0.5 m aperture Ritchey-Chretien optical system with a 508 mm primary mirror housed in a carbon-fiber truss design optical tube assembly and a two-lens field corrector. The equivalent focal ratio is F/8 and focal length is 4000 mm. The telescope is equipped with a motorized focuser and motorized primary and secondary mirrors covers.

The telescope is mounted on an ASA DDM100 equatorial mount equipped with direct drive motors and absolute encoders. A well-proven Astrosib ASD-4.5 all-sky dome (4.5 m) was chosen and will be mounted on an original hyperboloid 5.4 m high pier designed by INASAN (see Fig. 3).

The RCO observation station close to Kislovodsk will operate in a fully robotic mode with remote access by INASAN and IGA staff. For remote and

Figure 2. RC500 0.5 m aperture telescope for the second RCO station near Kislovodsk (Russia).

autonomous operations, the observation site has a set of equipment: weather stations, lightning detector, GPS/GLONASS receiver, all-sky camera and surveillance cameras. The observatory is controlled by a set of special software created by INASAN, which allows the control of all devices to perform scientific observations, data storage and data processing remotely.

4. Custom focal unit and scientific instruments

The second RCO station telescope most complicated part is its custom designed fully automated focal unit, which allows remote observations in both photomet-

Figure 3. 4.5 m Astrosib ASD-4.5 all-sky dome installed on a 5.4 m high pier at the INASAN observatory close to Kislovodsk (Russia).

ric and spectroscopic modes. The RC500 focal unit optical scheme, mechanical design and fabrication were done by INASAN. The majority of the focal unit components are off-the-shelf, which reduces cost and makes it easy to reproduce it for another telescope.

The RC500 custom-made focal unit main functions are:

– electromechanical switching between photometric and spectral modes of operation;

- electromechanical switching to calibrate spectrograph with calibration lamp;
- to alight two scientific instruments' focuses to avoid the telescope refocusing during switching between instruments;
- a possibility of installing an additional focal extender for the spectrograph;
- telescope guide camera and spectrograph slit viewing and guiding cameras;
- tip-tilp corrector for the spectrograph;
- high rigidity, mechanical stability of the entire structure and reliable fasteners;
- light tightness design;
- the ability to rotate and fix the entire assembly and its elements around the optical axis of the telescope, for accurate orientation of the spectrograph.

The main components of the custom-made focal unit are presented in Fig.4, 5 and the optical scheme is shown in Fig.6.

The 50 cm telescope has two main scientific instruments – a photometric imaging camera and medium resolution spectrograph, which are quickly interchangeable by the telescope's motorized folding mirror within 15 seconds. It allows for a very flexible observational program every night. Both photometric and spectroscopic modes of operation are available at any time without the need to modify the telescope's setup.

The main instrument for spectroscopic research is the Basic Echelle Spektrograph (BACHES). It is a compact, lightweight and inexpensive medium resolution (R=20000) Echelle spectrograph manufactured by Baader Planetarium GmbH, well suited for remote autonomous operation at a robotic observatory.

BACHES main parameters are:

- average spectral resolution: R$\sim$20000 with a slit of 25$\times$130 μm;
- spectral range: 3920-8000 Å continuously (depending on detector size);
- spectrograph efficiency: $\sim$27% at 5040 Å, total efficiency $\sim$11-13%;
- limiting magnitude: $\sim 10^m$ visual (SNR=20, 30 min. exposure);
- detector: a low noise and extra high sensitivity cooled back-illuminated sCMOS camera ZWO ASI294MM, Sony IMX492, sensor size 19.1$\times$13 mm;
- fiber feed calibration module: a Thorium-Argon hollow cathode lamp and Tungsten flat-field lamp.

BACHES allows the acquisition of spectra of an observed object as well as calibration spectra. To couple the spectrograph with the telescope, a simple

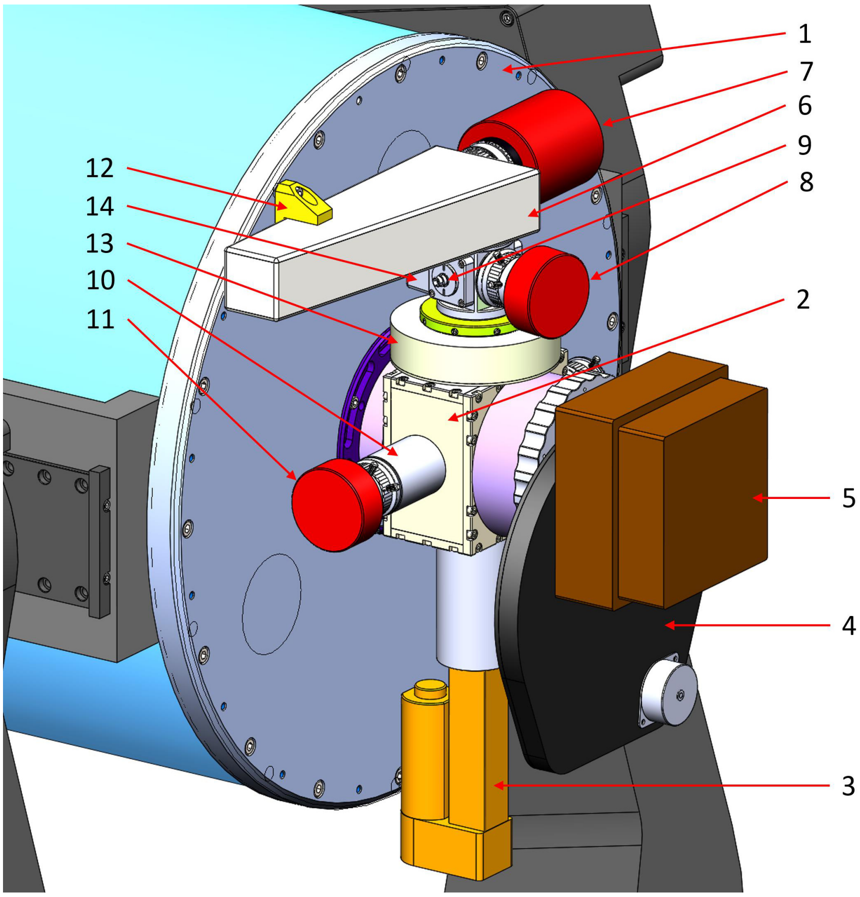

Figure 4. Custom focal unit main components: 1. Rear flange of the telescope; 2. Instrument selector; 3. Linear actuator, electromechanical driver of the diagonal mirror; 4. Filter wheel; 5. FLI Kepler 4040 camera; 6. BACHES spectrograph; 7. Spectrograph detector; 8. Spectrograph slit viewing and guiding camera; 9. Fiber-optic light input from the calibration module; 10. Off-axis guide camera focuser; 11. Off-axis guiding camera; 12. Additional mounting bracket for the spectrograph; 13. Active optics module for the spectrograph. 14. Driver of the diagonal mirror of the spectrograph calibration module.

achromatic telescope's focal extender Edmund Optics 62495 F/8 to F/10 is used. To allow for long spectroscopic observations with an exposure of up to 0.5 hours and more with minimum loss of light, BACHES is equipped with a tip-tilt active optics Starlight SXV-AO-USB module with a ZWO ASI178MM slit viewing and guiding camera. With a 0.5 m telescope, BACHES is capable of obtaining spectra of 10 mag targets with a SNR=20 for 30 minute exposures.

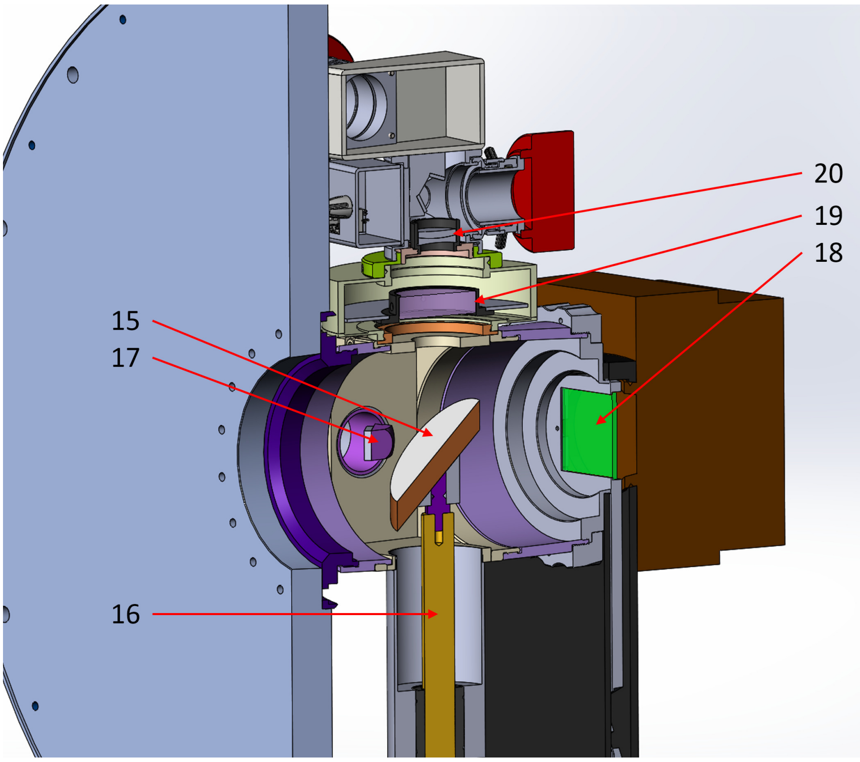

Figure 5. Custom focal unit main internal components: 15. Instrument selector diagonal mirror; 16. Linear actuator of the diagonal mirror, the position for spectral observations is shown; 17. Diagonal mirror of the side off-axis guider; 18. Scientific filter installed in the filter wheel; 19. Active optics module tip-tilt plate; 20. Focal extender for the spectrograph.

BACHES has been successfully used on the 1 m telescope at another INASAN observatory for several years. In 2024 it will be relocated to the new 0.5 m RCO telescope.

The second main 50 cm telescope scientific instrument is the sCMOS camera FLI Kepler 4040. The camera's main parameters are:

– sensor: GPIXEL GSENSE4040;

– format: 4096×4096 pixels;

– pixel size: 9 μm;

– full well capacity: 70000 e-;

– shutter type: rolling and mechanical;

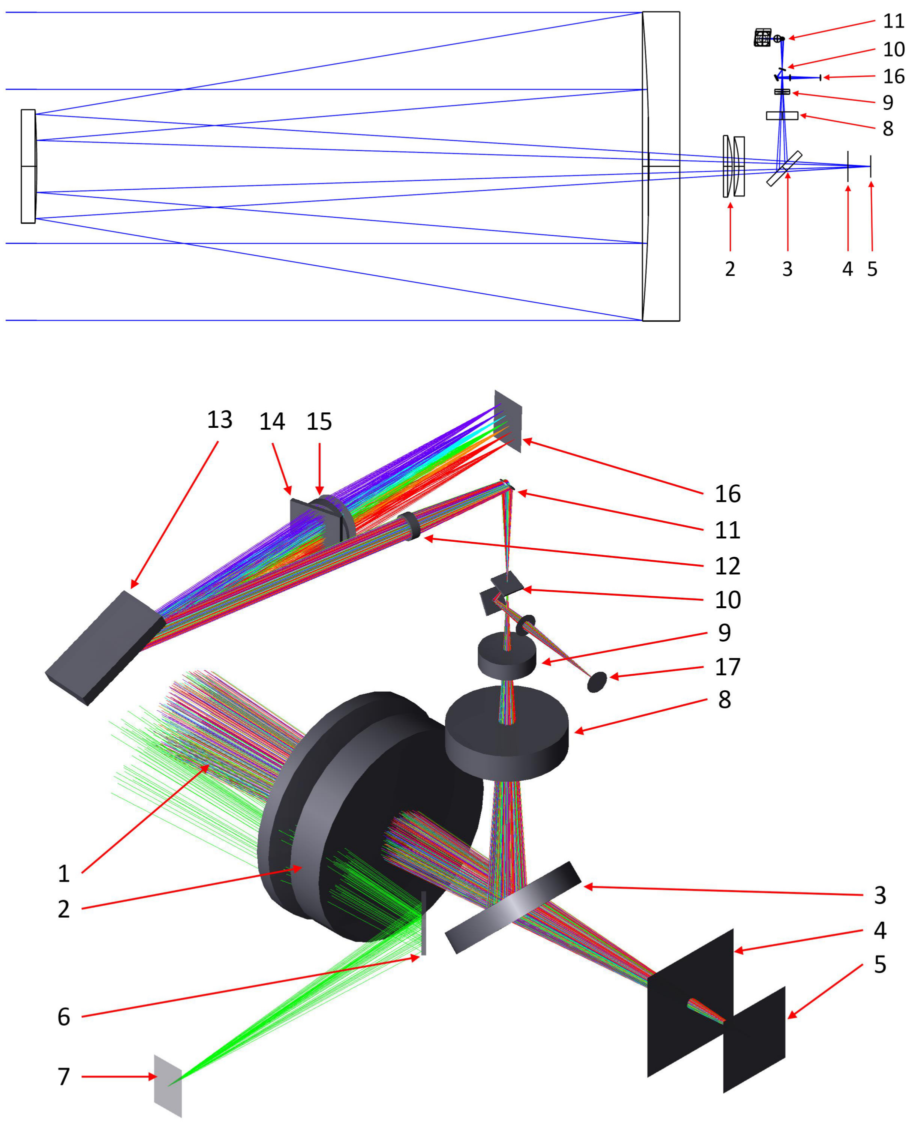

Figure 6. RC500 0.5 m aperture telescope and its focal plane instruments optical schemes: 1. Light from the telescope; 2. Telescope field corrector; 3. Diagonal switching mirror; 4. UBVRI filters; 5. Scientific FLI Kepler 4040 camera; 6. Main off-axis guide pick-off mirror; 7. Telescope off-axis guiding camera; 8. The tip-tilt plate of active optics module; 9. Focal extender; 10. Spectrograph entrance slit with a slit viewing mirror; 11. Spectrograph internal fold mirror; 12. Spectrograph collimator; 13. Spectrograph Echelle; 14. Spectrograph cross-disperser; 15. Spectrograph objective; 16. Spectrograph detector; 17. Spectrograph slit viewing and guiding camera.

– typical system noise: 3.7 e-;

– typical dark current: < 0.5 e-/pixel/sec at -30°C;

– typical non-linearity: < 1%.

The telescope focal unit has an off-axis guiding camera ZWO ASI178M with a Baader focuser 2458125. The camera is equipped with a FLI CFW5-7 filter wheel with 7 slots for photometric filters. In the first step, 5 filters of the standard Johnson-Cousins-Bessel system UBVRI will be installed. The sixth slot of the filter wheel will be used for broad-band imaging (integral light) to achieve maximum sensitivity of the telescope. In particular, this mode is efficient to search for new objects such as asteroids, comets and space debris. The seventh slot of the filter wheel will be reserved for future scientific observation programs.

5. Summary

The first 20 cm telescope of the Russian-Cuban RCO network has already been built in Havana (Cuba) and has been operating since 2021. The construction of the second 50 cm telescope close to Kislovodsk (Russia) is currently close to completion. Both telescopes are designed to operate in a fully robotic mode. It will allow Cuban and Russian astronomers to conduct scientific research remotely, both in photometric and spectroscopic modes.

It is expected to build the third 1 m telescope at Valle de Picadura (Cuba) before 2030, which will significantly improve the Russian-Cuban network functionality both in terms of global coverage and observation modes, including spectroscopic observations and more precise photometric observations.

Other telescopes worldwide, based on existing agreements, can be used for follow-up observations of the most interesting objects: INASAN's 2 m telescope at the Terskol observatory and INASAN's 1 m telescope, 0.5 m telescope of the Ussuri Department of the IAA RAS, several 0.5-1.5 m telescopes of the astronomical institutes of the Academy of Sciences of the Republic of Uzbekistan and the Republic of Tajikistan. All these observation sites together allow observations along an arc of 214 deg (or 14.3 h) in the northern hemisphere, which enables planning almost round-the-clock monitoring programs and alert observations from the above-mentioned observation sites.

International cooperation with other countries is highly welcomed for further expansion of the scientific potential of the optical telescope network.

Acknowledgements. The Russian team acknowledges financial support from the Ministry of Science and Higher Education of the Russian Federation (Agreement No. 075-15-2023-608 of August 30, 2023). The Cuban team acknowledges material, technical and financial support by the Ministry of Science, Technologies and Environment of the Republic of Cuba.

References

Bisikalo, D. V., Sachkov, M. E., Ibrahimov, M. A., et al., First Telescope of the Russian-Cuban Observatory. 2022, *Astronomy Reports*, **66**, 38, DOI:10.1134/S1063772922020019

Bisikalo, D. V., Savanov, I. S., Naroenkov, S. A., et al., Perspectives for Distributed Observations of Near-Earth Space Using a Russian-Cuban Observatory. 2018, *Astronomy Reports*, **62**, 367, DOI:10.1134/S1063772918060021

Ibrahimov, M., Bisikalo, D., Fateeva, A., Mata, R., & Pons, O., Prospects to observe comets and asteroids using Russian-Cuban Observatory. 2021, *Contributions of the Astronomical Observatory Skalnate Pleso*, **51**, 280, DOI:10.31577/caosp.2021.51.3.280

Ibrahimov, M., Shugarov, A., Shmagin, V., et al., INASAN 1-m Class Wide-Field Telescopes: Experience and Prospects. 2020, in *Ground-Based Astronomy in Russia. 21st Century*, ed. I. I. Romanyuk, I. A. Yakunin, A. F. Valeev, & D. O. Kudryavtsev, 174–176

Ibrahimov, M. A., INASAN network: wide-field 1m telescope creation experience. 2019, *INASAN Science Reports*, **4**, 93, DOI:10.26087/INASAN.2019.4.2.016

Kornilov, V., Kornilov, M., Voziakova, O., et al., Night-sky brightness and extinction at Mt Shatdzhatmaz. 2016a, *Monthly Notices of the RAS*, **462**, 4464, DOI:10.1093/mnras/stw1839

Kornilov, V. G., Kornilov, M. V., Shatsky, N. I., et al., Meteorological conditions at the Caucasus Observatory of the SAI MSU from the results of the 2007-2015 campaign. 2016b, *Astronomy Letters*, **42**, 616, DOI:10.1134/S1063773716090036

Naroenkov, S., Nalivkin, M., & Savanov, I., The first result of observations on the joint Russian-Cuban Observatory. 2022a, *Rev. Cubana Fis*, **39**, 115

Naroenkov, S. A., Savanov, I. S., Sachkov, M. E., & Nalivkin, M. A., Russian-Cuban Astronomical Observatory. The “First Light” and the First Results from the Observatory. 2022b, *Astronomy Reports*, **66**, 827, DOI:10.1134/S1063772922100109

Savanov, I. S., Naroenkov, S. A., Nalivkin, M. A., & Dmitrienko, E. S., Activity Cycles of the Star FK Com. 2023, *Astronomy Reports*, **67**, 1394, DOI:10.1134/S1063772923120089

Savanov, I. S., Naroenkov, S. A., Nalivkin, M. A., Tarasenkov, A. N., & Dmitrienko, E. S., ET Dra Activity According to Observations in 2018-2023. 2024, *Astronomy Reports*, **68**, 595

Shugarov, A., Shmagin, V., Shustov, B., et al., A 1-m Aperture Wide-Field Telescope with a 9x9k CMOS Detector. 2020, in *Ground-Based Astronomy in Russia. 21st Century*, ed. I. I. Romanyuk, I. A. Yakunin, A. F. Valeev, & D. O. Kudryavtsev, 177–181

Contrib. Astron. Obs. Skalnaté Pleso **55/1**, 18 – 37, (2025)
https://doi.org/10.31577/caosp.2025.55.1.18

Light curve analysis for the two eclipsing binary stars V869 Car and V2184 Sgr

M.A. Hanna[1], **A. Nakhlawy**[1], **M. Hayman**[2], **M.Y. Amin**[2], **H.R. Dwidar**[2], **M.A. El-Khamisy**[1] **and A. Essam**[1]

[1] *National Research Institute of Astronomy and Geophysics, Department of Astronomy, Helwan, Cairo, Egypt (E-mail: magdyh_nriag06@yahoo.com)*

[2] *Cairo University, Faculty of Science, Department of Astronomy and Meteorology, Egypt*

Received: August 31, 2024; Accepted: December 9, 2024

Abstract. We present the first light curve analysis for two detached eccentric eclipsing Algol-type binaries V869 Car and V2184 Sgr, using the PHOEBE code. The stars were selected from the PZP catalogue. The light curve for V869 Car is from the OgleII project. For V2184 Sgr, we analyzed two available light curves from the ASAS and the TESS mission. We determined 8 new times of minima for V 2184 Sgr and preliminary orbital and physical parameters for both systems. The analysis shows e, ω(rad) and q_{ph} equal to 0.070(1), 2.976(52) and 0.951(8) for V869 Car, while 0.4896(5), 5.750(2) and 0.9004(70) for V2184 Sgr. The analysis shows that both stars are of late F-Spectral types in which one may expect magnetic activity or star spots due to their convective envelopes.

Key words: binaries: eclipsing – stars: eccentric – apsidal motion – V869 Car – V2184 Sgr

1. Introduction

Contact and semi-detached binaries of short orbital periods are distinguished by their circular orbits due to the large mutual tidal interaction and the mass transfer between their components. On the other hand, detached eccentric binaries are with longer orbital periods and characterized by the phenomenon of apsidal motion due to the mutual tidal interaction between their components.

Apsidal motion in detached binary systems, driven by tidal forces, rotational deformation, dynamical interaction of triples, including so-called dynamical delays (see, e.g., Rappaport et al. (2023, 2024); Borkovits et al. (2015); Borkovits & Mitnyan (2023)) and relativistic effects, involves the gradual precession of the orbit's major axis. This phenomenon is crucial for constraining the internal structure of the stars' components in these systems, offering valuable information through the internal structure constant, k_2. However, it is important to note that the apsidal motion measurements provide a weighted average mean of k_2, reflecting combined contributions rather than detailed individual internal structures. For a deeper understanding, see studies by Petrova & Orlov (2002) and Claret & Gimenez (1989). Systems with eccentric orbits exhibit unique tidal effects due to the varying gravitational forces throughout their orbits. These interactions can cause significant stellar distortions and periodic pulsations, particularly evident in heartbeat stars. These stars, named for their distinct light curve patterns that resemble a heartbeat, showcase how tidal forces can induce oscillations and variations in stellar temperatures and shapes, especially at periastron. Notable examples from the Kepler mission, such as KOI-54, have provided profound insights into these tidal interactions.

Observational data of long-period binaries using normal ground-based telescopes are relatively limited due to the difficulties facing observers to covering their full light curves. This has led to a lack of data available for binaries of this class. Fortunately, during the past three decades, great advances in instruments and many satellites and automated ground telescopes have obtained high-quality observations. Examples include the Kepler space telescope, the Optical Gravitational Lensing Experiment (OGLE), All Sky Automated Survey (ASAS), Super-WASP survey, and the Transiting Exoplanet Survey Satellite (TESS) (Ricker et al., 2015). These large-scale photometric surveys have reported tens of thousands of new eclipsing binaries in our Galaxy and in other nearby galaxies (Kim et al., 2018). Hence, analysis of these data is necessary and required. Consequently, several authors have compiled catalogues for detached eclipsing binary stars that show apsidal line rotation. Examples of such catalogues include Petrova & Orlov (1999), Hegedüs et al. (2005), Bulut & Demircan (2007), Prša et al. (2011), Slawson et al. (2011), Kirk et al. (2016) and Kim et al. (2018). For a preferred summary of most of these catalogues, see Kjurkchieva et al. (2017).

Several researchers have investigated individual eccentric binaries, e.g., Frandsen et al. (2013), Gaulme et al. (2013, 2014, 2016), Borkovits et al. (2014), Maceroni et al. (2014), and Rawls et al. (2016). Kjurkchieva & Vasileva (2015a,b) modeled several systems from the Kepler catalogue of eccentric binaries and obtained their orbital and stellar parameters using the PHOEBE code. In the present work, we aim to follow their procedure in analyzing the light curves of two long-period eccentric eclipsing binaries (EEB) that were observed from different sources such as OGLE, ASAS, and TESS.

In the next section, we provide information and a brief description of the available data of the two systems. Section 3 deals with the analysis of light curves using the PHOEBE code, while Section 4 deals with the results and discussion.

2. Source of data

From the Peremennye Zvezdy Prilozhenie catalogue (volume 12 and volume 11), we selected two detached systems, OGLEII CAR-SC1 46493 (= V869 Car) and ASAS 194617-3724 (= V2184 Sgr = TIC 299888115), as their light curves exhibit a secondary minimum deviation from the phase value 0.5 (Fig. 4 &

Table 1. Stars magnitudes and effective temperatures from different sources.

Name	G	J	H	K	B	V	$T_{eff.}$
V869 Car	-	14.46[1]	13.96[1]	13.63[1]	-	-	6264[4]
V2184 Sgr	12.5688[2]	11.547[2]	11.318[3]	11.240[3]	13.29[1]	12.70[1]	6183[4]

[1] Gaia Collaboration (2018), yCat. 1345.
[2] Cutri et al. (2003), yCat. 2246.
[3] Høg et al. (2000).
[4] Bai et al. (2019) .

Fig. 5). Also, we included the recent light curve observed for V2184 Sgr via TESS in June/July 2019 (Fig. 6). The magnitudes in different bands for both systems and the effective temperature $T_{1eff.}$ were collected from various sources and are listed in Table 1.

2.1. V869 Car

Huemmerich & Bernhard (2012) classified the star OGLEII CAR-SC1 46493 ($\alpha_{2000} = 11^h 05^m\ 59^s.24$, $\delta_{2000} = -61°50^{'}58^{''}.9$) as an Algol eccentric eclipsing binary with a secondary eclipse at 0.45 phase. They recorded the line elements,

$$HJD(Min.I) = 2450551^d.628 + 2^d.23281\ E. \tag{1}$$

The star was then named V869 Carina, by Kazarovets et al. (2015), in the GCVS.

2.2. V2184 Sgr

The variable nature of V2184 Sgr (TIC 299888115) ($\alpha_{2000} = 19^h 46^m 17^s.49$, $\delta_{2000} = -37°24^{'}52^{''}.7$) was discovered by Hoffmeister (1963). It was included in the GCVS as an EA-type star without light elements. Later, Kreiner (2004) introduced the light elements:

$$HJDMinI = 24\,52505^d.1325 + 16^d.495833\ E, \tag{2}$$

$$HJDMinII = 24\,52509^d.0615 + 16^d.494994\ E. \tag{3}$$

Other light elements were given by Paschke & Brát (2006):

$$HJD(MinI) = 24\,53214^d.456 + 16^d.496\ E. \tag{4}$$

$$HJD(MinII) = 24\,53630^d.645 + 16^d.496\ E. \tag{5}$$

Kim et al. (2018) presented the light elements,

$$HJD(MinI) = 24\,53212^d.280 + 16^d.49541\ E. \tag{6}$$

While the international Variable Star index (VSX) gave the light elements,

$$HJD(MinI) = 24\,53614^{d}.205 + 16^{d}.496\ E. \tag{7}$$

Seven times of minima (Table 2) were taken from the online O-C gateway website (Paschke & Brát, 2006). Besides, we deduced 8 new minima times from the light curves of the TESS mission (Ricker et al., 2022) by using the AVE program that uses Barbera (1996) method. The O-C residuals are calculated using equation (6) of Kim et al. (2018), and plotted in Fig.1.

Table 2. Time of minima for V2184 Sgr.

HJD (+2400000)	O-C (day)	Type	Method	Ref.
53214.4565	2.4565	P	pe V	[1]
53713.2249	-1.8851	S	pe V	[1]
53940.2470	2.4490	P	pe V	[1]
53944.1188	-1.9269	S	pe V	[1]
54055.7606	2.4947	p	pe V	[1]
54142.0650	-1.9257	S	pe V	[1]
54897.0283	2.4965	P	pe V	[1]
58658.00532±0.00014	2.5200	P	CCD (I)	[2]
58661.82509±0.00011	-1.9079	S	CCD (I)	[2]
58674.50037±0.00027	2.5197	P	CCD (I)	[2]
58678.32066±0.00028	-1.9078	S	CCD (I)	[2]
59037.40158±0.40158	2.5218	P	CCD (I)	[2]
59041.22167±0.00008	-1.9058	S	CCD (I)	[2]
59053.89716±0.00009	2.5220	P	CCD (I)	[2]
59057.71695±0.00015	-1.9059	S	CCD (I)	[2]

[1] Paschke & Brát (2006).

[2] present work obtained from TESS LCs.

Recently, in 2019 and 2020, the Transiting Exoplanet Survey Satellite (TESS) provided 4 new light curves for V2184 Sgr. Due to the high accuracy of the data we aimed to analyze the first LC observed during June-July 2019 too, and compare results obtained from both ASAS and TESS observations.

3. Light curve analysis

The morphology of the light curves of both systems shows that the secondary eclipse has shifted from phase 0.5 and exhibits constant brightness outside the eclipses. Therefore, to proceed with the analysis of the light curves using the PHOEBE code (Prša & Zwitter, 2005) we chose the detached mode. In analyzing

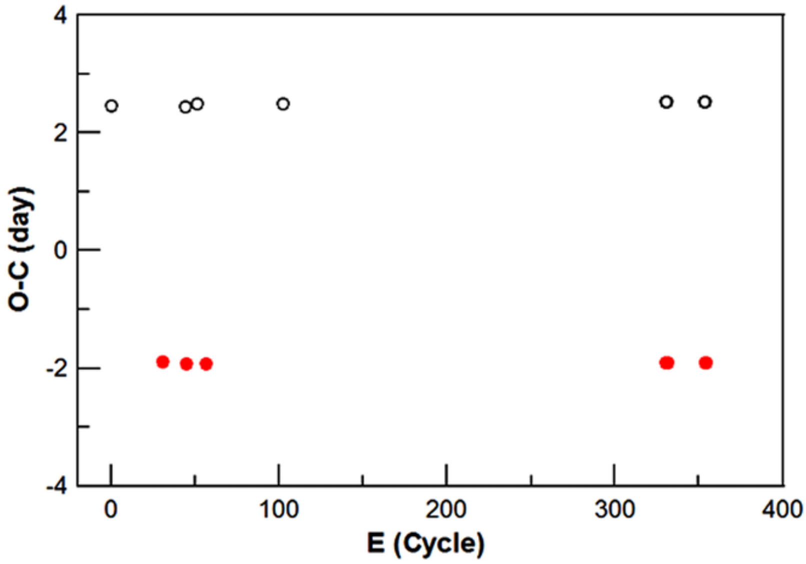

Figure 1. The O-C diagram of V 2184 Sgr; open circles stand for primary minima, while dots for secondaries.

the light curve we kept the primary component effective temperature, T_1, as a constant and run the program to fit T_2 (Zasche, 2016). We used $T_{1\ eff.} = 6264\ K$ for V869 Car and $6183\ K$ for V2184 Sgr, both values were taken from the Gaia catalogue (Bai et al., 2019). Bolometric albedo and gravity-darkening coefficients were also used as constant input parameters. After Lucy (1967) and Ruciński (1973), one can obtain the gravity-darkening coefficient. The effective temperature, $T_{1\ eff.}$, for both systems is below $7200\ K$, thus, when considering convective envelope components, the gravity-darkening coefficient is assumed to be $g_1 = g_2 = 0.32$ and the bolometric albedo $A_1 = A_2 = 0.5$ (Zasche, 2016). To proceed to the solution of the light curve for such binaries without wasting time, we have to calculate roughly the values of orbital eccentricity, $e_\circ$, and the longitude of periastron, $\omega_\circ$. This can be done by solving the following two equations which are the approximate equations (9.25) and (9.37) given by Kopal (1978),

$$e_o \cos \omega_o = \frac{1}{2} \cdot \pi[(\phi_2 - \phi_1) - 0.5], \tag{8}$$

$$e_o \sin \omega_o = (W_2 - W_1)/(W_2 + W_1), \tag{9}$$

where $e_\circ$ and $\omega_\circ$ are the orbital eccentricity and longitude of periastron; W_1 and W_2 are the duration widths of the primary and secondary minima (in phase

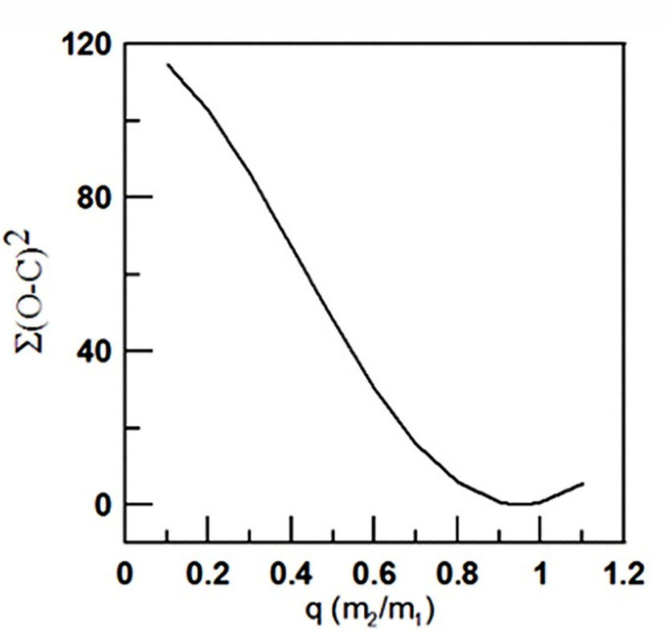

Figure 2. The $q_{ph} - \sum(O-C)^2$ relation for V869 Car.

units); ϕ_2 is the phase of the secondary minimum, while $\phi_1 = 0$ (see Table 3). One has to note that equation (9) is valid for orbits close to edge-on (inclination close to 90°). The inclination of long-period eclipsing binaries is close to 90° because the eclipse would not occur for low inclination angles. One can easily estimate the minimum inclination angle i for eclipses to occur as cos $i < r_1 + r_2$, where r_1 and r_2 are the fractional radii of the components ($r_{1,2} = R_{1,2}/a$), noting that their values are very small in detached long period binaries (Table 4). We have obtained $e_\circ = 0.0732$ and $\omega_\circ = 2.829$ (rad.) for V869 Car. Also for V2184 Sgr$_{ASAS}$, we determined $e_\circ = 0.4512$ and $\omega_\circ = 5.910$ (rad) and for V2184 Sgr$_{TESS}$, we determined $e_\circ = 0.4720$ and $\omega_\circ = 5.823$ (rad). Both $e_\circ$ and $\omega_\circ$ are used as input raw parameters for PHOEBE.

In the absence of spectroscopic observations, the mass ratio q $(= m_2/m_1)$ can be estimated from photometric data by following a q-search procedure (see, e.g., Djurašević et al. (2016), Awadalla et al. (2016), El-Sadek et al. (2019) and Hanna et al. (2024)). However, at the beginning of the analysis, we kept the mass ratio value at one. This approach is justified because both binaries are well-detached and the elliptical differences outside of their eclipse are nearly negligible (Zasche et al., 2018). Wyithe & Wilson (2002) indicated that in the

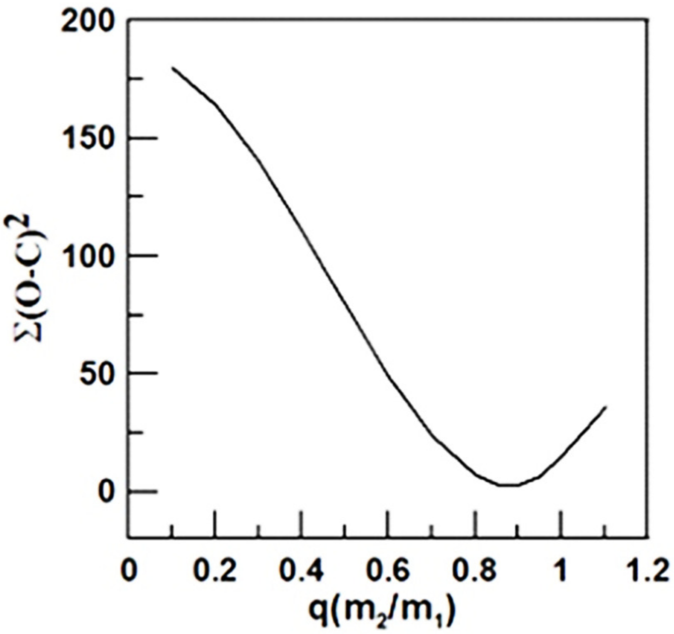

Figure 3. The $q_{ph} - \sum(O-C)^2$ relation for V2184 Sgr.

case of a detached binary, the effect of the mass ratio, generally, during the analysis of the LC can be effective if the system has a very low mass ratio or if one of the components is too advanced (the case in which the radius R increases to half the total separation, a). The preliminary tests show that no component of our two binaries has its fractional radius $r_i(= R_i/a)$ larger than 0.2, see Graczyk (2003). Hence, we started the program with $q = 1$ and after arriving at the best fit solution, we ran the program including fitting q.

We validated our final estimate of q by the well-known q-search procedure by constructing the relationship between the sum of squared weight deviation $(O-C)^2$ and q (Fig. 2 & 3). This method requires creating a series of simplified models with different values of the mass ratio q, chosen to cover a reasonable range. In this study, the search is carried out from $q = 0.1$ to 1.1. We determined the photometric mass ratio, q_{ph}, to be 0.951(8) for V869 Car, 0.885(13) for V2184 Sgr_{ASAS} and 0.9004(70) for V2184 Sgr_{TESS}. For the analysis, we followed the same implementation of Zasche (2016). We considered the effective temperature of the primary component, $T_{1\ eff.}$, and the mass ratio, $q_{ph} = 1$, as constant parameters. We first started by adjusting the inclination, i, with the

Table 3. The measured parameters from the light curves. The eccentricity (e_o) and periastron angle (ω_o) are calculated to be the initial input orbital parameters to PHOEBE.

	W_1	W_2	ϕ_2	e_o	ω_o (Rad.)
V869 Car_{OGLE}	0.1250	0.1210	0.4560	0.0732	2.829
V2184 Sgr_{ASAS}	0.0310	0.0223	0.7677	0.4512	5.910
V2184 Sgr_{TESS}	0.0328	0.0214	0.7689	0.4720	5.823

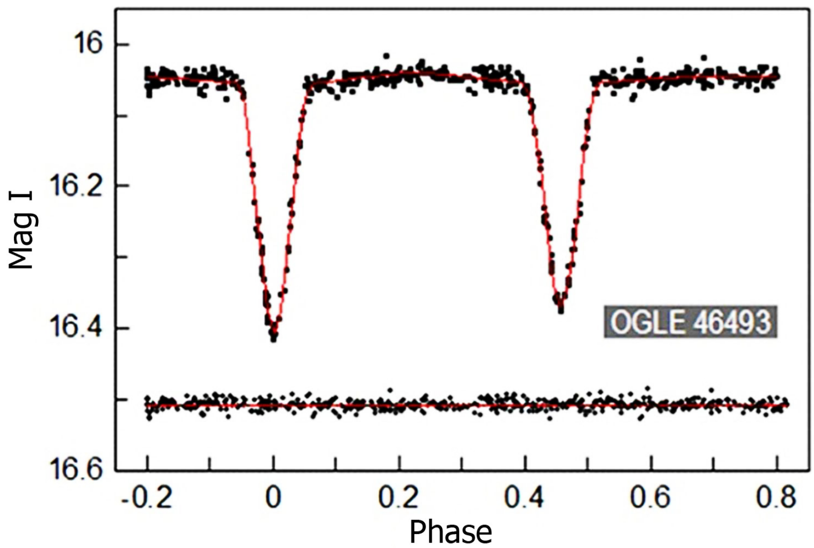

Figure 4. Top: The V869 Car light curve (dots) and its fit in the red solid line; bottom: corresponding residuals (moved vertically to save space).

primary luminosity. We then included the surface potentials of the primary and secondary components (Ω_1 & Ω_2) in the process of the fitting, in an effort to come up with a better approach. We then included the eccentricity, periastron longitude and the phase shift as variable values in the analysis. We followed the fitting step by step until the solution converged giving an acceptable good fit. Moreover, we include the mass ratio in the fitting process and continue till we reach the best fit with the lowest cost function value. The final solution set parameters along with standard errors are listed in Table 4, while the synthetic light curves extracted with these parameters are plotted as red solid lines in Fig. 4, Fig. 5 and Fig. 6 along with residuals at the bottom of each figure.

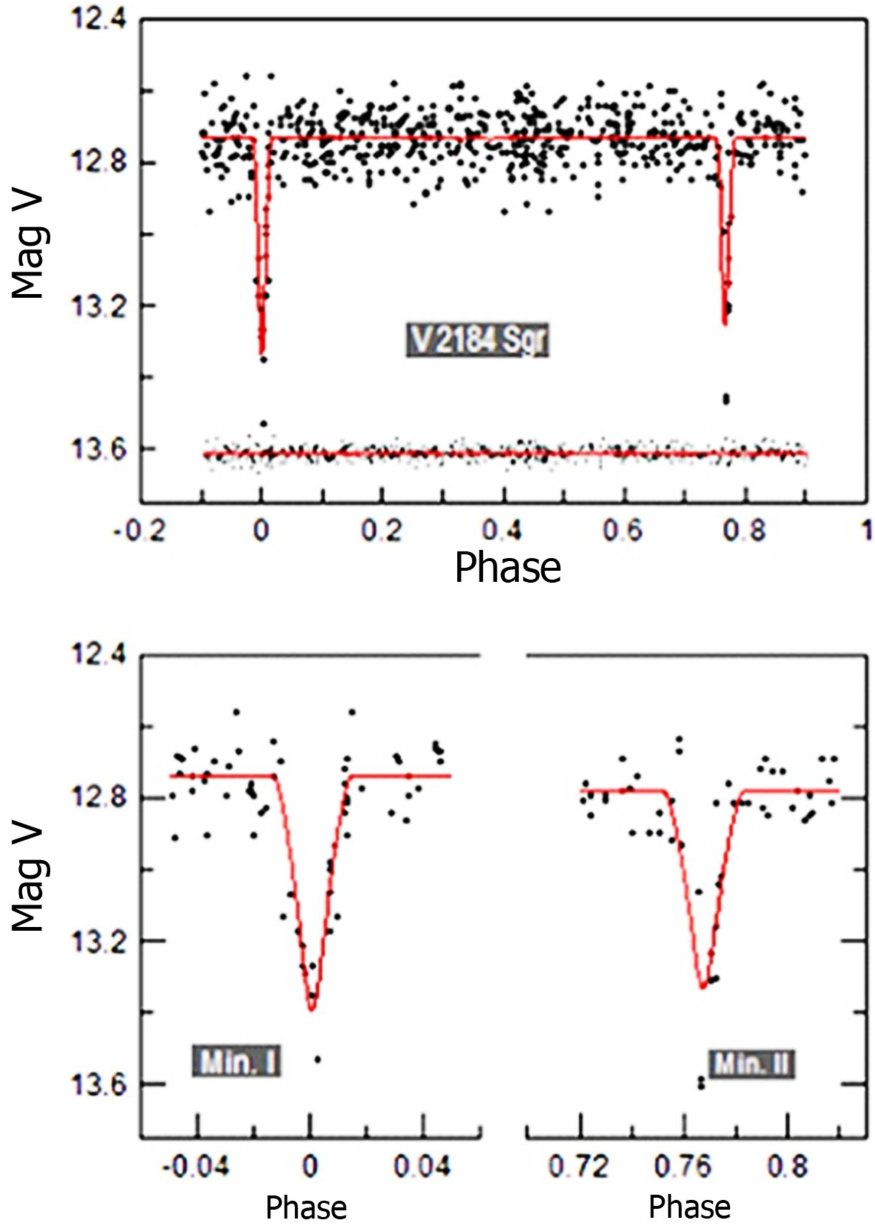

Figure 5. Top panel: V2184 Sgr$_{ASAS}$ light curve (dots) and its fit in the red solid line with the corresponding residuals (moved vertically to save space). Bottom panel: The two minima in a different scale just for clarity.

Table 4. Orbital and physical parameters of V869 Car and V2184 Sgr

Parameters	V869 Car	V2184 Sgr$_{ASAS}$	V2184 Sgr$_{TESS}$
Wavelength	8000 Å	5500 Å	8100 Å I central band=7865 Å
T_o (day)	2450551.628	2453614.205	2458663.999 ±0.000102
P (day)	2.23281 ± 0.00002	16.4960 ± 0.00003	16.4959 ± 0.00001
e	0.07023 ±0.001	0.43348 ±0.0004	0.48963 ±0.0005
ω (rad)	2.976 ±0.052	6.270 ±0.011	5.75 ±0.001
$T_{1eff.}$ (K)	6264 (fixed)	6183 (fixed)	6183 (fixed)
$T_{2eff.}$ (K)	6069.381 ±19.031	6088 ±134	6130 ±17
Phase shift	0.02103 ±0.00016	0.13446 ±0.00009	0.1587 ±0.000006
i (°)	81°.528 ±0.063	89°.6 ±0.022	89°.72 ±0.014
q	0.951 ±0.008	0.886 ±0.013	0.885 ±0.007
$l_1/(l_1+l_2)$	0.4807 ±0.0971	0.47020 ±0.1831	0.49854 ±0.019
$l_2/(l_1+l_2)$	0.5193 ±0.0971	0.52979 ±0.1831	0.50145 ±0.019
r_1	0.1900	0.0419	0.0426
r_2	0.1868	0.0419	0.0425
x_1	0.369 ±0.085	0.552 ±0.123	0.686 ±0.013
x_2	0.385 ±0.096	0.749 ±0.213	0.687 ±0.03
Ω_1	6.479 ±0.034	23.8110 ±0.139	26.724 ±0.230
Ω_2	5.9402 ±0.0303	18.152 ±0.173	23.580 ±0.2218
f_1	-0.375	-0.732	-0.721
f_2	-0.320	-0.653	-0.635
ALB1	0.5	0.5	0.5
ALB2	0.5	0.5	0.5
g_1	0.32	0.32	0.32
g_2	0.32	0.32	0.32

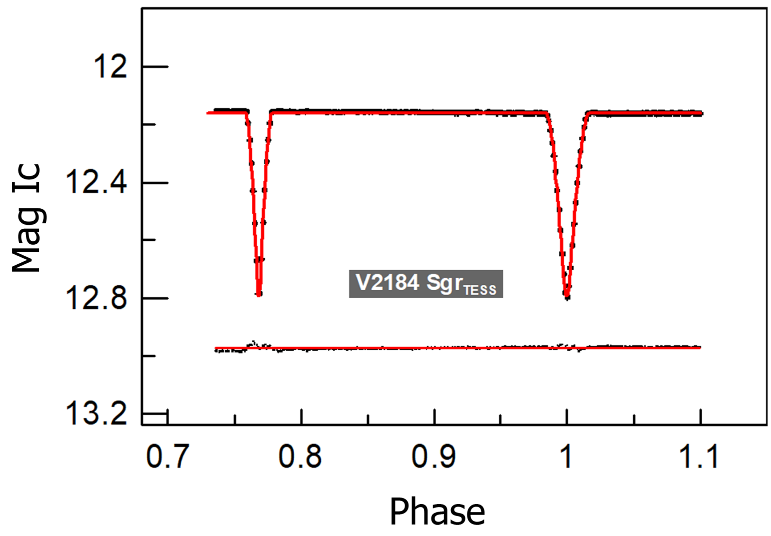

Figure 6. Top: V2184 Sgr$_{TESS}$ light curve (dots) and its fit in the red solid line with the corresponding residuals (moved vertically to save space).

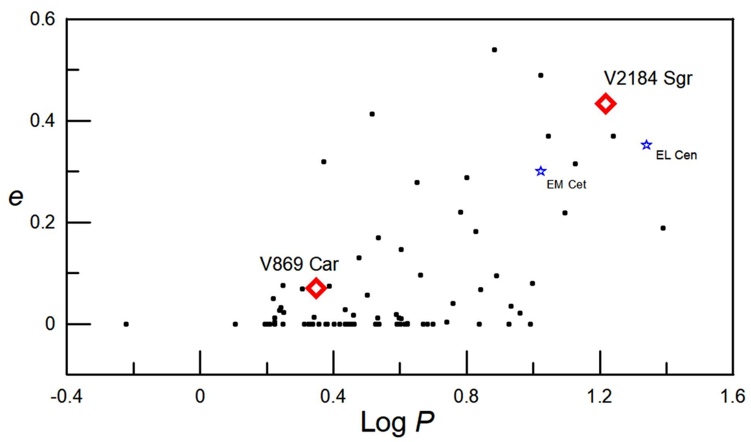

Figure 7. The (e-Log$P$) plane for a binary sample of 78 well-studied binaries listed in Mayer & Hanna (1991) (dots). The present two targets V2184 Sgr and V869 Car are denoted by the red square symbols, while the blue star symbols represent EM Cet and EL Cen that were studied recently by Hanna et al. (2024).

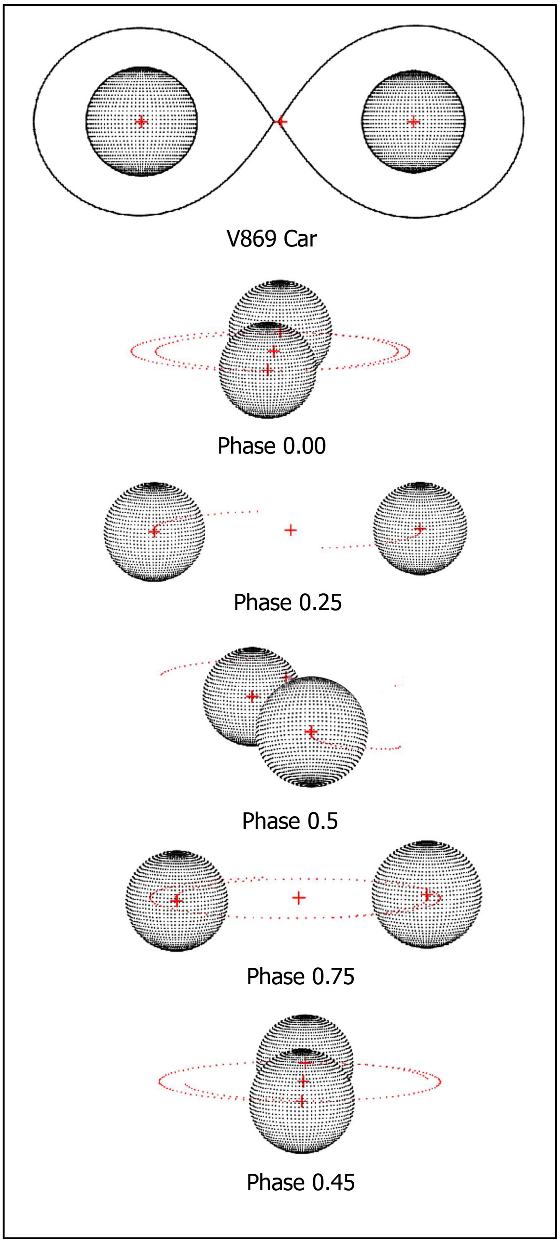

Figure 8. Up: The Roche Lobe configuration of V869 Car. Bottom: The orbital phases represent the situation in different phases 0.0, 0.25, 0.5, 0.75. The phase 0.45 shows the shape at the secondary eclipse.

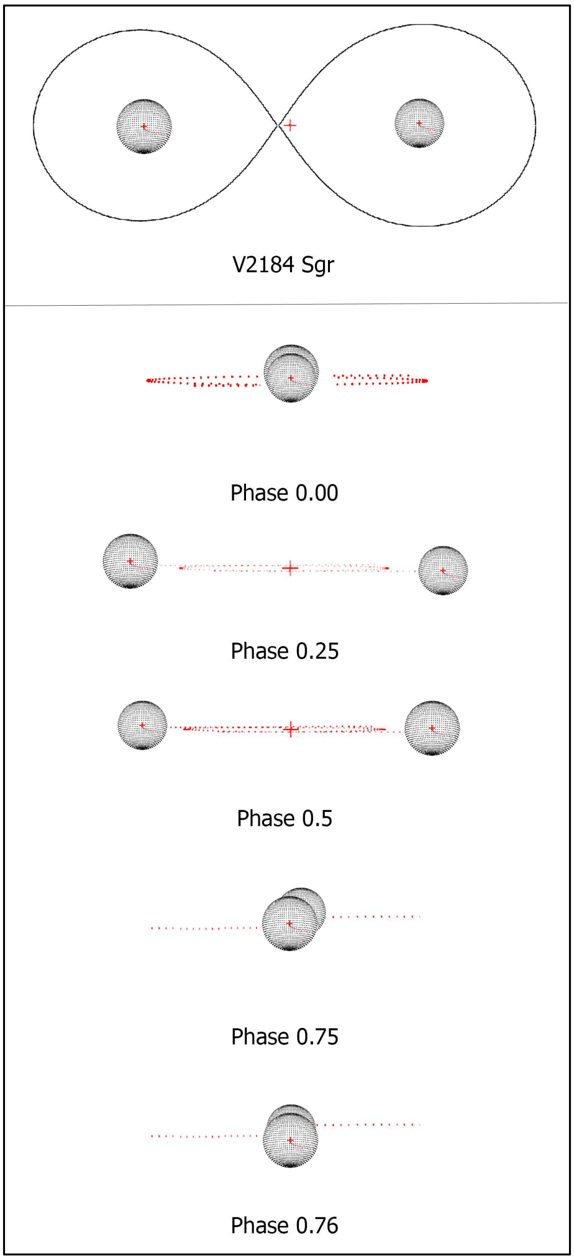

Figure 9. Up: The Roche Lobe configuration of V2184 Sgr. Bottom: The orbital phases represent the situation in different phases 0.0, 0.25, 0.5, 0.75. The phase 0.76 shows the shape at the secondary eclipse.

Table 5. Orbital and physical parameters of V869 Car and V2184 Sgr.

Star Name	Comp.	M $M_\odot$	R $R_\odot$	T_{eff} K	L $L_\odot$	M (bol.)	Log g	Sp.type
V869 Car	Pri.	1.250 (2)	1.33 (02)	6264	2.70 (16)	3.65 (03)	4.28 (01)	F8
	Sec.	1.19 (10)	1.27 (10)	6069 (19)	1.95 (55)	4.88 (04)	4.34 (04)	F9
V2184 Sgr (ASAS)	Pri	1.23 (03)	1.31 (03)	6183	2.389 (60)	3.79 (3)	4.290 (2)	F8
	Sec.	1.203 (8)	1.282 (7)	6088 (124)	2.148 (61)	3.906 (30)	4.302 (2)	F9
V2184 Sgr (TESS)	Pri.	1.230 (08)	1.312 (7)	6183	2.389 (60)	3.79 (3)	4.296 (2)	F8
	Sec.	1.210 (8)	1.295 (7)	6130 (17)	2.25 (6)	3.85 (3)	4.298 (2)	F9

4. Discussion and conclusion

Eclipsing binaries, especially those with eccentric orbits, are fundamental stellar systems that provide both the physical parameters (e.g., mass, radius, temperature and luminosity) and orbital parameters (e.g., period, eccentricity, and longitude of periastron). These two sets of parameters allow testing different tidal theories (e.g., Alexander's weak friction theory, Alexander (1973); Zahn's theory, Zahn (1977) and Tassoul's theory, Tassoul (1988)), deducing the apsidal motion parameters and calculating the synchronization & circularization timescales Hanna (1993) & Hanna et al. (1998). Hence, studying the evolution and internal structure of stars.

– On analyzing the light curve of V2184 Sgr of the ASAS (Fig. 5), one may notice that the fit at the minima does not adequately match the data. This has been observed in other similar studies. More than 13 out of 54 systems studied by Zasche et al. (2018) did not adequately describe the data, e.g., CzeV 688, CzeV 364, CD-33 2771, V611 Pup, TYC 8603-723-1, PS Vul and V839 Cep. They stated that this may be due to the fact that the mass ratio is based on the assumption of a main sequence of star components and that they may be giants or some over-luminous stars according to their effective temperatures. Zasche (2016) also reported that this may only be due to the limitations of the software itself and the limited physics built into it. However, basically in the analysis, we keep the light curves so that the cost function does not drop dramatically, only varies around some value and shows no further progression. Also, even the residual values are distributed relatively symmetrically around the zero line and no systematic deviations appear there.

- On comparing the obtained two sets of parameters of V2184 Sgr$^{ASAS}_{TESS}$ (see, Table 4), one can notice that the differences are in the range of the estimated errors for each parameter. For example, the eccentricity, longitude of periastron and inclination are quite similar, while there are small differences in some other parameters such as T_2, surface potentials Ω_1 & Ω_2 and limb darkening x_1 & x_2. However, it is preferable to consider the results of the TESS light curve since its morphological profile is better than the scattered light curve of ASAS, and it was observed over a shorter interval of time.

- The obtained orbital inclination from the analysis of the two light curves of V2184 Sgr are nearly the same, within the error range ($i_{ASAS} = 89^{\circ}.60 \pm 0.022$ and $i_{TESS} = 89^{\circ}.72 \pm 0.014$). Both values are very close to 90°, which is typically expected for eclipses of binaries with orbital periods greater than eight days (Kjurkchieva & Vasileva, 2015b).

- We deduced the spectral type of V869 Car and V2184 Sgr using the tables given by Cox (2000). The effective temperatures, $T_{1,2\ eff}$ for V869 Car are 6264 K & 6069(19)K, which correspond to spectral types $F8$ & $F9$. For V2184 Sgr$_{ASAS}$, $T_{1,2\ eff}$ are 6183 & 6088(134) K which correspond to $F8$ & $F9$, while for V2184 Sgr$_{TESS}$, $T_{1,2\ eff}$ are 6183 K & 6130(17) K which correspond to $F8$ & $F9$, respectively. This result is expected, suggesting that both stars are essentially solar-type main sequence stars.

- It is worth noticing that the light curve by TESS (Fig. 6) is clearly of very good quality, as compared with the scattered ASAS light curve (Fig. 5), and consequently, its fit could be better than that of ASAS. The ASAS observations cover about 7.2 years while the light curve of TESS is continuous and covering the two minima (prim. & sec.) of the light curve only in about 11 successive days.

- It is important to note that the solutions presented in Table 4 are still only preliminary results based on photometry, and the individual parameter errors based on the errors provided by the PHOEBE software.

- We have determined 8 new times of primary and secondary minima from the four TESS light curves, all are listed in Table 2 together with the available minima times in the O-C gateway (Paschke & Brát, 2006) . We attempted to study the period variation due to the apsidal motion by the $O - C$ plot analysis, but we could not come up with an acceptable solution due to the lack of minima time available.

- The absolute physical parameters of the components were calculated using the empirical relations adopted by Harmanec (1988) and listed in Table 5.

- The main choice of the two systems under analysis is simple and does not depend on their location or brightness. The criterion based on analyzing new light curves for systems that have not been studied before, since our main goal is to expand the present set of eclipsing binaries in the period-eccentricity diagram. Another criterion for our selection is systems with good phase light curves, i.e., photometry must cover the entire light curve and especially the duration and depths of both eclipses.
  We have constructed the e-Log$P$ plane to check the location of our two targets among a set of 78 detached eclipsing binaries brighter than 9^m in maxima. They are well-studied binaries collected from the GCVS (58 systems) together with other fainter detached binaries with well determined parameters, as compiled by Harmanec (1988) as well as several others from different sources. All are listed in Mayer & Hanna (1991). We have plotted our two targets together with another two systems EM Cet & EL Cen of our recent paper (Hanna et al., 2024). The four systems follow the same trend distribution of the group as seen in the plot (Fig. 7).

- Using the PHOEBE software, we determined the orbital elements and stellar parameters of the two detached systems V869 Car and V2184 Sgr. The analysis shows that both stars are of late spectral types in which one may expect magnetic activity or star spots due to their convective envelopes.

- The geometrical configuration for both systems and the model solution at different orbital phases using the Binary Maker program (Version 3) are also illustrated by Figures 8 & 9.

- The light curves' morphology clearly show that both systems are detached eccentric eclipsing binaries, and the analysis contributed for orbital eccentricities equal to ($e = 0.4896 \pm 0.0018$) and ($e = 0.0702 \pm 0.001$) for V2184 Sgr and V869 Car, respectively.

Acknowledgements. This research makes use of the SIMBAD and Vizier data base, the NASA Astrophysics Data Service, the PZP catalogue, the O-C gateway, the All Sky Automated Survey (ASAS) data, the Transiting Exoplanet Satellite mission (TESS) data and the PHOEBE software in the light curve analysis. The authors are grateful to an anonymous referee for valuable notes and propositions.

References

Alexander, M. E., The Weak Friction Approximation and Tidal Evolution in Close Binary Systems. 1973, *Astrophysics and Space Science*, **23**, 459, DOI:10.1007/BF00645172

Awadalla, N. S., Hanna, M. A., Ismail, M. N., Hassan, I. A., & Elkhamisy, M. A., New CCD Observations and the First Photometric Study of the Contact Binary AP UMi. 2016, *Journal of Korean Astronomical Society*, **49**, 65, DOI:10.5303/JKAS.2016.49.3.065

Bai, Y., Liu, J., Bai, Z., Wang, S., & Fan, D., Machine-learning Regression of Stellar Effective Temperatures in the Second Gaia Data Release. 2019, *Astronomical Journal*, **158**, 93, DOI:10.3847/1538-3881/ab3048

Barbera, R. 1996, AVE (Analisis de Variabilidad Estelar) Version 2.5

Borkovits, T., Derekas, A., Fuller, J., et al., HD 183648: a Kepler eclipsing binary with anomalous ellipsoidal variations and a pulsating component. 2014, *Monthly Notices of the RAS*, **443**, 3068, DOI:10.1093/mnras/stu1379

Borkovits, T. & Mitnyan, T., Observational Detection of Higher-Order Secular Perturbations in Tight Hierarchical Triple Stars. 2023, *Universe*, **9**, 485, DOI:10.3390/universe9110485

Borkovits, T., Rappaport, S., Hajdu, T., & Sztakovics, J., Eclipse timing variation analyses of eccentric binaries with close tertiaries in the Kepler field. 2015, *Monthly Notices of the RAS*, **448**, 946, DOI:10.1093/mnras/stv015

Bulut, İ. & Demircan, O., A new catalogue of eclipsing binary stars with eccentric orbits*. 2007, *Monthly Notices of the RAS*, **378**, 179, DOI:10.1111/j.1365-2966.2007.11756.x

Claret, A. & Gimenez, A., The moment of inertia of main sequence stars. 1989, *Astronomy and Astrophysics, Supplement*, **81**, 37

Cox, A. N. 2000, *Allen's astrophysical quantities*

Cutri, R. M., Skrutskie, M. F., van Dyk, S., et al. 2003, VizieR Online Data Catalog: 2MASS All-Sky Catalog of Point Sources (Cutri+ 2003), VizieR On-line Data Catalog: II/246. Originally published in: 2003yCat.2246....0C

Djurašević, G., Essam, A., Latković, O., et al., A Photometric Study of Four Recently Discovered Contact Binaries: 1SWASP J064501.21+342154.9, 1SWASP J155822.10-025604.8, 1SWASP J212808.86+151622.0, and UCAC4 436-062932. 2016, *Astronomical Journal*, **152**, 57, DOI:10.3847/0004-6256/152/3/57

El-Sadek, M. A., Djurašević, G., Essam, A., et al., A photometric study of two recently discovered, contact binaries-II: UCAC4 479-113658 and UCAC4 479-113711. 2019, *New Astronomy*, **69**, 21, DOI:10.1016/j.newast.2018.11.006

Frandsen, S., Lehmann, H., Hekker, S., et al., KIC 8410637: a 408-day period eclipsing binary containing a pulsating giant star. 2013, *Astronomy and Astrophysics*, **556**, A138, DOI:10.1051/0004-6361/201321817

Gaia Collaboration. 2018, VizieR Online Data Catalog: Gaia DR2 (Gaia Collaboration, 2018), VizieR On-line Data Catalog: I/345. Originally published in: 2018A&A...616A...1G

Gaulme, P., Jackiewicz, J., Appourchaux, T., & Mosser, B., Surface Activity and Oscillation Amplitudes of Red Giants in Eclipsing Binaries. 2014, *Astrophysical Journal*, **785**, 5, DOI:10.1088/0004-637X/785/1/5

Gaulme, P., McKeever, J., Jackiewicz, J., et al., Testing the Asteroseismic Scaling Relations for Red Giants with Eclipsing Binaries Observed by Kepler. 2016, *Astrophysical Journal*, **832**, 121, DOI:10.3847/0004-637X/832/2/121

Gaulme, P., McKeever, J., Rawls, M. L., et al., Red Giants in Eclipsing Binary and Multiple-star Systems: Modeling and Asteroseismic Analysis of 70 Candidates from Kepler Data. 2013, *Astrophysical Journal*, **767**, 82, DOI:10.1088/0004-637X/767/1/82

Graczyk, D., Light-curve solutions for bright detached eclipsing binaries in the Small Magellanic Cloud: absolute dimensions and distance indicators. 2003, *Monthly Notices of the RAS*, **342**, 1334, DOI:10.1046/j.1365-8711.2003.06636.x

Hanna, M. 1993, Binary Stars and their Orbital Eccentricities, Unpublished, Charles University, Praha, Czech Republic., PhD thesis

Hanna, M., Mayer, P., & Hanna, Y., Circularization of Binary Orbits. 1998, *Astrophysics and Space Science*, **262**, 171

Hanna, M. A., Nakhlawy, A., Hayman, M., et al., Light curve analysis for the two eclipsing binary stars EM Cet and EL Cen. 2024, *Contributions of the Astronomical Observatory Skalnate Pleso*, **54**, 5, DOI:10.31577/caosp.2024.54.3.5

Harmanec, P., Stellar Masses and Radii Based on Modern Binary Data. 1988, *Bulletin of the Astronomical Institutes of Czechoslovakia*, **39**, 329

Hegedüs, T., Giménez, A., & Claret, A., Eccentric Eclipsing Binary Systems - the Up-Dated Catalogue. 2005, in Astronomical Society of the Pacific Conference Series, Vol. **333**, *Tidal Evolution and Oscillations in Binary Stars*, ed. A. Claret, A. Giménez, & J. P. Zahn, 88

Hoffmeister, C., Veraenderliche Sterne am Sudhimmel. 1963, *Veroeffentlichungen der Sternwarte Sonneberg*, **6**, 1

Høg, E., Fabricius, C., Makarov, V. V., et al., The Tycho-2 catalogue of the 2.5 million brightest stars. 2000, *Astronomy and Astrophysics*, **355**, L27

Huemmerich, S. & Bernhard, K., New Eclipsing Binaries in the OGLE-II Database (Part 1). The Carina Galactic Disk Fields. 2012, *Peremennye Zvezdy Prilozhenie*, **12**, 11

Kazarovets, E. V., Samus, N. N., Durlevich, O. V., Kireeva, N. N., & Pastukhova, E. N., The 81st Name-List of Variable Stars. Part I - RA 00h to 17h30. 2015, *Information Bulletin on Variable Stars*, **6151**, 1

Kim, C. H., , J. M., Zakrzewski, B., et al., A Comprehensive Catalog of Galactic Eclipsing Binary Stars with Eccentric Orbits Based on Eclipse Timing Diagrams. 2018, *Astrophysical Journal, Supplement*, **235**, 41, DOI:10.3847/1538-4365/aab7ef

Kirk, B., Conroy, K., Prša, A., et al., Kepler Eclipsing Binary Stars. VII. The Catalog of Eclipsing Binaries Found in the Entire Kepler Data Set. 2016, *Astronomical Journal*, **151**, 68, DOI:10.3847/0004-6256/151/3/68

Kjurkchieva, D. & Vasileva, D., Light Curve Solutions of Ten Eccentric Kepler Binaries, Three of them with Tidally Induced Humps. 2015a, *Publications of the Astron. Soc. of Australia*

Kjurkchieva, D. & Vasileva, D., Light curve solutions of the eccentric Kepler binaries KIC 11619964 and KIC 7118545 and mid-eclipse brightening of KIC 11619964. 2015b, *Bulgarian Astronomical Journal*

Kjurkchieva, D., Vasileva, D., & Atanasova, T., Orbital Parameters of the Eclipsing Detached Kepler Binaries with Eccentric Orbits. 2017, *Astronomical Journal*, **154**, 105, DOI:10.3847/1538-3881/aa83b3

Kopal, Z. 1978, *Dynamics of close binary systems(Book). Dordrecht, D. Reidel Publishing Co. (Astrophysics and Space Science Library), 68, 524*, DOI:10.1007/978-94-009-9780-6

Kreiner, J. M., Up-to-Date Linear Elements of Eclipsing Binaries. 2004, *Acta Astronomica*, **54**, 207

Lucy, L. B., Gravity-Darkening for Stars with Convective Envelopes. 1967, *Zeitschrift fuer Astrophysik*, **65**, 89

Maceroni, C., Lehmann, H., da Silva, R., et al., KIC 3858884: a hybrid δ Scuti pulsator in a highly eccentric eclipsing binary. 2014, *Astronomy and Astrophysics*, **563**, A59, DOI:10.1051/0004-6361/201322871

Mayer, P. & Hanna, M. A. M., Eclipsing Binaries with Eccentric Orbits. 1991, *Bulletin of the Astronomical Institutes of Czechoslovakia*, **42**, 98

Paschke, A. & Brát, L., O-C Gateway, a Collection of Minima Timings. 2006, *Open European Journal on Variable Stars*, **23**, 13

Petrova, A. V. & Orlov, V. V., Apsidal Motion in Double Stars. I. Catalog. 1999, *Astronomical Journal*, **117**, 587, DOI:10.1086/300671

Petrova, A. V. & Orlov, V. V., Apsidal Motion in Detached Binary Stars: Comparison of Theory and Observations. 2002, *Astrophysics*, **45**, 334, DOI:10.1023/A:1020143617776

Prša, A., Batalha, N., Slawson, R. W., et al., Kepler Eclipsing Binary Stars. I. Catalog and Principal Characterization of 1879 Eclipsing Binaries in the First Data Release. 2011, *Astronomical Journal*, **141**, 83, DOI:10.1088/0004-6256/141/3/83

Prša, A. & Zwitter, T., A Computational Guide to Physics of Eclipsing Binaries. I. Demonstrations and Perspectives. 2005, *Astrophysical Journal*, **628**, 426, DOI:10.1086/430591

Rappaport, S. A., Borkovits, T., Gagliano, R., et al., A study of nine compact triply eclipsing triples. 2023, *Monthly Notices of the RAS*, **521**, 558, DOI:10.1093/mnras/stad367

Rappaport, S. A., Borkovits, T., Mitnyan, T., et al., Seven new triply eclipsing triple star systems. 2024, *Astronomy and Astrophysics*, **686**, A27, DOI:10.1051/0004-6361/202449273

Rawls, M. L., Gaulme, P., McKeever, J., et al., KIC 9246715: The Double Red Giant Eclipsing Binary with Odd Oscillations. 2016, *Astrophysical Journal*, **818**, 108, DOI:10.3847/0004-637X/818/2/108

Ricker, G. R., Winn, J., & Vanderspek, R., The Transiting Exoplanet Survey Satellite (TESS). in , *Bulletin of the American Astronomical Society*, Vol. **54**, 406.02

Ricker, G. R., Winn, J. N., Vanderspek, R., et al., Transiting Exoplanet Survey Satellite (TESS). 2015, *Journal of Astronomical Telescopes, Instruments, and Systems*, **1**, 014003, DOI:10.1117/1.JATIS.1.1.014003

Ruciński, S. M., The Photometric Proximity Effects in Close Binary Systems. VI. The Exact Solution for the Source Function in Monodirectional Illumination of the Grey Atmosphere. 1973, *Acta Astronomica*, **23**, 301

Slawson, R. W., Prša, A., Welsh, W. F., et al., Kepler Eclipsing Binary Stars. II. 2165 Eclipsing Binaries in the Second Data Release. 2011, *Astronomical Journal*, **142**, 160, DOI:10.1088/0004-6256/142/5/160

Tassoul, J.-L., On Orbital Circularization in Detached Close Binaries. 1988, *Astrophysical Journal, Letters*, **324**, L71, DOI:10.1086/185094

Wyithe, J. S. B. & Wilson, R. E., Photometric Solutions for Semidetached Eclipsing Binaries: Selection of Distance Indicators in the Small Magellanic Cloud. 2002, *Astrophysical Journal*, **571**, 293, DOI:10.1086/339877

Zahn, J. P., Tidal friction in close binary systems. 1977, *Astronomy and Astrophysics*, **57**, 383

Zasche, P., PHOEBE - step by step manual. 2016, *Open European Journal on Variable Stars*, **176**, 10

Zasche, P., Wolf, M., Uhlař, R., et al., The first study of 54 new eccentric eclipsing binaries in our Galaxy. 2018, *Astronomy and Astrophysics*, **619**, A85, DOI:10.1051/0004-6361/201832793

Contrib. Astron. Obs. Skalnaté Pleso **55/1**, 38 – 59, (2025)
https://doi.org/10.31577/caosp.2025.55.1.38

Kinematics of high-velocity stars utilizing LAMOST and Gaia DR3 archives within 100 kpc

W.H. Elsanhoury

Physics Department, College of Science, Northern Border University, Arar, Saudi Arabia (E-mail: elsanhoury@nbu.edu.sa)

Received: December 14, 2024; Accepted: January 21, 2025

Abstract. The kinematic parameters identified from high-velocity stars situated within $\sim$ 100 kpc are examined and analyzed. We included three high-velocity programs comprising 591, 87, and 519 stars as a function of distances ranging from 0.10 kpc to nearly 109 kpc. In this analysis, we will determine the spatial velocities (U, V, W) in galactic coordinates along with their velocity dispersion (σ_1, σ_2, σ_3), the convergent point (A_o, D_o) and, therefore, the solar motion ($S_\odot$). In conclusion, we are calculating the first Oort constant ($A = 11.94 \pm 0.29$ km s^{-1} kpc^{-1}) and the second one (i.e., $B = -17.78 \pm 0.24$ km s^{-1} kpc^{-1}), the angular rotation rate $|A–B| = 25.07 \pm 5.01$ km s^{-1} kpc^{-1}, and the average rotational velocity $V_o = 243.72 \pm 15.61$ km s^{-1}.

Key words: High-velocity stars – Gaia DR3 – Kinematics – Oort constants.

1. Introduction

The stars known as high-velocity stars (HiVels) travel through space at substantially faster rates than the average Milky Way (MW) Galaxy star. These objects are special in astronomy study since they can reach speeds of thousands or even hundreds of kilometers per second. In the disk region, almost all the stars in our Galaxy rotate around the galactic center at a normal velocity of 200–240 km s^{-1} (Bovy et al., 2012; Huang et al., 2016; Eilers et al., 2019). An alternative indirect estimate of both the circular velocity (V_o) and the escape velocity (V_{esc}) at which the stars in the solar neighborhood would have sufficient energy to completely escape from our Galaxy's gravitational field can be obtained from the kinematic properties of the halo-population stars that have been observed to have the largest space velocities to the Sun (i.e., the extreme HiVels).

Including the Gaia DR3, Large Sky Area Multi-Object Fiber Telescope (LAMOST, Cui et al. (2012)) galactic surveys, and spectroscopic observations from large-scale galactic surveys (SEGUE, (Yanny et al., 2009; Rockosi et al., 2022)) have demonstrated the existence of HiVels in our Galaxy. Among these, a few are even hypervelocity stars (HVSs), meaning that their V_{esc} are smaller than their overall galactocentric velocities (V_{GSR}), and almost all HiVels have low luminosity ($M_G \sim 10$ mag).

In the halo, they exhibit tens of kilometers per second (Xue et al., 2008; Huang et al., 2016), especially when a star approaches or even exceeds the Galaxy's escape velocity at its position. HiVels indicate the presence of extreme dynamical and astrophysical processes (Hills, 1988; Yu & Tremaine, 2003; Bromley et al., 2006; Abadi et al., 2009; O'Leary & Loeb, 2008; Capuzzo-Dolcetta & Fragione, 2015; Marchetti et al., 2019). The finding of such rare objects offers a valuable tool for investigating the MW's mass distribution, particularly its dark component (Gnedin et al., 2005; Rossi et al., 2017; Contigiani et al., 2019), because they travel large distances across it (Gnedin et al., 2005; Kenyon et al., 2008), and their trajectories can also be used to probe the shape of the Galaxy's dark matter halo (Bromley et al., 2006; Yu & Madau, 2007). The study of stellar motion and the dynamics of the MW Galaxy reveals a relationship between HiVels and the Oort constants (A & B), where HiVels offer special test cases for comprehending extreme stellar motions both inside and outside of the Galaxy.

HiVels and HVSs can be divided into four subclasses, each with a distinct origin of these high velocities; i) black hole ejection (BHE): As a result of tidal interaction between a close stellar binary system and a supermassive black hole (SMBH) in the Galaxy, a process known as the "Hills mechanism," the so-called HVSs (with velocities even greater than 1000 km s^{-1}) were first predicted from theoretical arguments of Hills (1988). Extending the Hills mechanism allows for the ejection of HVSs and HiVels, ii) supernova explosions (SNEs) can cause significant disruption to binary systems and induce their companion stars to become HiVels or HVSs. Examples of such explosions include core-collapse and thermonuclear supernova explosions (SNe) (Blaauw, 1961; Portegies Zwart, 2000; Justham et al., 2009; Wang & Han, 2009; Pakmor et al., 2013; Zubovas et al., 2013; Shen et al., 2018; Neunteufel, 2020; Bauer et al., 2019). Generally, stars with velocities of no more than 300–400 km s^{-1} cannot be ejected by core-collapse SNEs (Portegies Zwart, 2000), iii) dynamical ejection mechanism (DEM), in which three or four-body interaction of stars (and black holes) in high-density environment ejects a runaway star (Poveda et al., 1967). This process involves the expulsion of runaway stars from young stellar clusters because of close stellar interactions. This mechanism often achieves a maximum kick velocity of around 300–400 km s^{-1}, which is the result of collisions between two close binaries (Leonard & Duncan, 1990; Leonard, 1991; Gvaramadze et al., 2009), and iv) tidal stripping from dwarf galaxies (TSD): In this scenario, stars can be rapidly removed from a dwarf Galaxy that is pericentrically passing through a region where the MW gravity field is causing tidal disruption (Abadi et al., 2009). According to Piffl et al. (2011), runway stars in this mechanism must be expelled by a large dwarf Galaxy ($> 10^{10} M_\odot$).

The study aims to examine and report the spatial structures, kinematics of the HiVels, including their velocity ellipsoid motion characteristics, parameters characterizing the local rotational properties of our Galaxy such as Oort's constants A and B. In the context of our ongoing investigations into stellar associations, we present velocity ellipsoid parameters for three Program stars as a function of distances (d), i.e., Program I (591 stars; $0.10 \leq d(\mathrm{kpc}) \leq 15.40$), Program II (87 stars; $0.30 \leq d(\mathrm{kpc}) \leq 108.64$), and Program III (519 stars; $0.29 \leq d(\mathrm{kpc}) \leq 16.44$). Moreover, determination of the equatorial coordinates for convergent points (i.e., A_o, D_o) with AD-chart method. Finally, we computed the MW Galaxy's local differential rotation close to the Sun, i.e., the Oort constants (A & B) based on observed velocities of three considered Program stars.

The remainder of this article is structured as follows: Section 2 provides the selected data considered in this analysis. Section 3 details the computational methods, including velocity ellipsoid parameters and the convergent point Section 4 deals with the galactic rotational constants. We close finally with discussion and conclusions in Section 5.

2. Selected data

The Large Sky Area Multi-Object Fiber Spectroscopic Telescope (LAMOST), also named the "Guo Shou Jing" Telescope (Cui et al., 2012) is a 4-m Schmidt spectroscopic survey telescope specifically developed to study four thousand targets per exposure in a field of view roughly 5^o in diameter (Cui et al., 2012; Luo et al., 2012; Feltzing et al., 2014). LAMOST spectra have a resolution of $\sim$1800 with a wavelength range of 3800–9100 $\mathring{A}$. In March 2020, 10,608,416 spectra in DR7[1] (Lei et al., 2020) were made accessible by LAMOST.

The third major data release from the European Space Agency's (ESA) Gaia mission, which aspires to provide the most precise three-dimensional map of the Milky Way, is called Gaia Data Release 3 (hereafter DR3) (Gaia Collaboration et al., 2023). Gaia is an astrometry expedition that was launched in 2013 to determine the locations, distances, movements, and other characteristics of over one billion stars and other celestial objects. Released on June 13, 2022, DR3 represents a major update to the earlier Gaia data releases (DR1 and DR2) in understanding stars' physical characteristics and chemical makeup. Moreover, detailed astrometric parameters like equatorial coordinate system (α, δ), parallaxes (π; mas), movements within the MW as the well-known proper motion (PM; mas yr^{-1}) components in right ascension and declination ($\mu_\alpha \cos\delta$, μ_δ) for roughly 470 million stars, and radial velocities (V_r; km s^{-1}) for 34 million stars, DR3 is a rich source of stellar data and provides photometric across three broadband filters: the G band (330–1050 nm), the Blue Prism (G_{BP}: 330–680 nm), and the Red Prism (G_{RP}: 630–1050 nm) for sources brighter than 21 mag. Common errors in the photometric observations throughout these three bands with $G \leq 20$ magnitudes are approximately 0.30 magnitude and increase for fainter stars (approaching $G = 21$). DR3 can measure PM for bright stars (G

[1] `http://dr7.lamost.org/`

≤ 15) with remarkable accuracy, frequently to within ~ 0.02 to 0.03 mas yr^{-1}. With uncertainties of about 1.00 mas yr^{-1} or exceed for fainter stars ($G = 20$), but it still yields useful motion data. The uncertainty limit in parallax is about 0.02 to 0.03 mas for $G < 15$ mag, ~ 0.07 mas for $G = 17$ mag, ~ 0.50 mas for $G = 20$ mag, and ~ 1.30 mas for $G = 21$ (Gaia Collaboration et al., 2023). The astrometric accuracy of DR3 is significantly better than that of DR2, with PM accuracy being doubled and parallax accuracy being roughly 1.5 times higher. Furthermore, astrometric inaccuracies in parallax measurements were reduced by 30-40%, while accurate motion measurements were improved by 2.5 times.

Li et al. (2021) reported on approximately 591 HiVels in the galactic halos with three-dimensional velocities in the galactic rest frame larger than 445 km s^{-1} that were chosen from over 10 million spectra of Data Release 7 of the Large Sky Area Multi-object Fiber Spectroscopic Telescope (LAMOST DR7) and the second Gaia data release (Gaia DR2, Gaia Collaboration et al. (2016)).

According to the fifth data release of the V_r Experiment survey (RAVE DR5, (Kunder et al., 2017)), the twelfth data release of the Sloan Digital Sky Survey (SDSS DR12, (Alam et al., 2015)), the eighth data release of the Large Sky Area Multi-Object Fiber Telescope (LAMOST DR8, (Wang et al., 2022)), sixteenth data release of The Apache Point Observatory Galactic Evolution Experiment (APOGEE DR16, (Majewski et al., 2017)), second data release of the Galactic Archaeology (GALAH DR2, (De Silva et al., 2015)), and Early Data Release 3 (Gaia EDR3), Li et al. (2023) present about 88 HiVels by large-scale galactic surveys.

With crossmatch between DR3 and precise V_r with other large-scale galactic surveys, such as GALAH DR3 (De Silva et al., 2015; Buder et al., 2021), LAMOST DR10 (Yanny et al., 2009; Zhao et al., 2012), RAVE DR6 (Steinmetz et al., 2020), APOGEE DR17 (Majewski et al., 2017), Liao et al. (2024) present about 591 HiVels of the Large Magellanic Cloud (LMC).

In what follows, we report in our analysis three Programs (I, II, and III) of halo HiVels as a function of distances and lags between a few parsecs till ~ 100 kpc.

The most recent data from DR3 was used to update and enhance Programs I, II, and III. To ensure data consistency, crossmatches were carried out using software that was based on the Tool for OPerations on Catalogues And Tables (TOPCAT) and Starlink Tables Infrastructure Library (STIL; Taylor (2005)). This tool has several options for modifying astronomical catalogs and is especially reliable when examining tabular data within a given range ($0 < x < 1$).

(i) The Program I mainly aims to comprehend the galactic and kinematic characteristics of about 591 HiVels (Li et al., 2021) with LAMOST and Gaia DR3 located ($0.10 \leq d(\text{kpc}) \leq 15.40$).

(ii) Program II was set for 87 HiVels who are ejected from the galactic center with large-scale galactic surveys (Li et al., 2023) with DR3, LAMOST, SDSS, and other large-scale surveys combining astrometric and spectroscopic data within ($0.30 \leq d(\text{kpc}) \leq 108.64$). The missing one of 88 stars is HVS23 ($\alpha = 240^o.537580$, $\delta = 0^o.912272$) into which there is no Gaia DR3 identification number and no proper motions data in both directions, therefore, we neglect it from this Program set.

(iii) Program III was set and updated via DR3 sources for 519 HiVels influenced by LMC's gravitational potential (Liao et al., 2024) in the range of ($0.29 \leq d(\text{kpc}) \leq 16.44$).

Table 1 presents the fundamental parameters of these three Programs of HiVels (Li et al., 2021, 2023; Liao et al., 2024), respectively. The distribution of selected stars across the sky is shown in Figure 1 with almost random directions of velocity vectors. Figure 2 presents the V_r distribution as a function of galactic longitude (l^o) for all halo HiVels observed in our considered three Programs (I, II, and III).

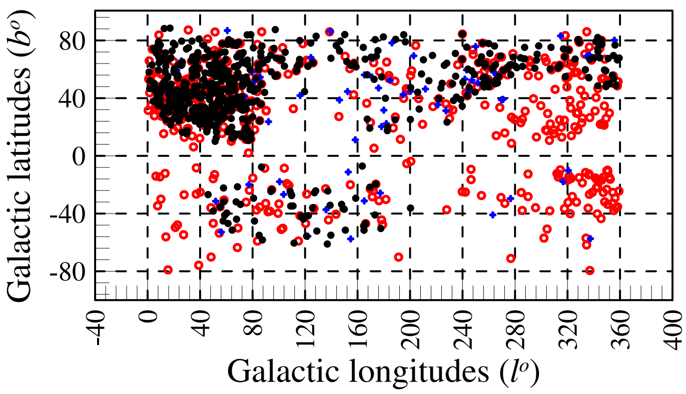

Figure 1. Distribution of HiVels in the galactic coordinate system (l, b). Program I: black closed circles (591 stars), Program II: blue closed pluses (87 stars), and Program III: red open circles (519 stars).

3. VEPs and CP

3.1. Velocity ellipsoid parameters (VEPs)

A equatorial-galactic transformation matrix based on the SPECFIND v2.0 catalog of radio continuum spectra (see Eq. (14); Liu et al. (2011)) was used to derive the spatial velocity components (U, V, and W; km s^{-1}) of HiVels in galactic coordinates with the aid of the calculated space velocity components (V_x, V_y, and V_z; km s^{-1}) at distances (d_i; pc) from the Sun as given in Eqs. (4), (5), and (6). Therefore,

Table 1. The fundamental parameters of the three Programs I, II, and III of HiVels adopted by Li et al. (2021, 2023), and Liao et al. (2024), respectively.

No.	Gaia DR3 ID	Ra. deg.	Dec. deg.	$V_r \pm \sigma_{V_r}$ km s^{-1}
Program I: N = 591 stars; $0.10 \leq d$(kpc) ≤ 15.40				
1	1383279090527227264	240.3375	41.1668	-184 ± 5.00
2	1570348658847157888	193.4372	55.0581	-230 ± 15.00
3	966594450238136704	102.4834	46.8368	-80 ± 6.00
.	.	.	.	.
.	.	.	.	.
.	.	.	.	.
591	1272009269712167680	229.6719	28.3365	-147 ± 12.00
Program II: N = 87 stars; $0.30 \leq d$(kpc) ≤ 108.64				
1	255667999133782348	12.3624	7.1290	-345.37 ± 9.48
2	2801887851883799936	12.5096	21.4207	-32.94 ± 14.38
3	2510946771548268160	29.3032	1.1937	217 ± 2.26
.	.	.	.	.
.	.	.	.	.
.	.	.	.	.
87	2872564390598678016	352.2706	33.0032	237.3 ± 6.40
Program III: N = 519 stars; $0.29 \leq d$(kpc) ≤ 16.44				
1	6087590373666222080	201.7684	-44.5009	328.84 ± 1.19
2	6098873935647575552	220.6412	-44.5675	163.15 ± 0.71
3	6135358205355639424	193.4286	-44.9466	203.66 ± 0.32
.	.	.	.	.
.	.	.	.	.
.	.	.	.	.
519	4421621689671197568	229.5736	2.1771	-54.16 ± 0.82

$$U = -0.0518807421V_x - 0.8722226427V_y - 0.4863497200V_z, \tag{1}$$

$$V = 0.4846922369V_x - 0.4477920852V_y + 0.7513692061V_z, \tag{2}$$

$$W = -0.8731447899V_x - 0.1967483417V_y + 0.4459913295V_z, \tag{3}$$

where

$$V_x = -4.74 d_i \mu_\alpha \cos\delta \sin\alpha - 4.74 d_i \mu_\delta \sin\delta \cos\alpha + V_r \cos\delta \cos\alpha, \tag{4}$$

$$V_y = +4.74 d_i \mu_\alpha \cos\delta \cos\alpha - 4.74 d_i \mu_\delta \sin\delta \sin\alpha + V_r \cos\delta \sin\alpha, \tag{5}$$

$$V_z = +4.74 d_i \mu_\delta \cos\delta + V_r \sin\delta. \tag{6}$$

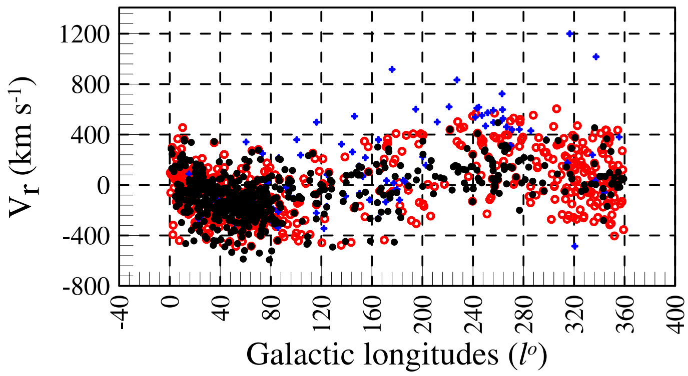

Figure 2. Distribution of (V_r; km s^{-1}) for three Program HiVels as a function of their galactic longitudes (l^o). Program I: black closed circles (591 stars), Program II: blue closed pluses (87 stars), and Program III: red open circles (519 stars).

In what follows, we estimate the velocities' dispersion (σ_1, σ_2, and σ_3; km s^{-1}) using the following equations to specify VEPs as described in the literature (Elsanhoury, 2024; Elsanhoury & Al-Johani, 2023):

$$\begin{aligned} \sigma_1 &= \sqrt{2\rho^{\frac{1}{3}} \cos\tfrac{\phi}{3} - \tfrac{k_1}{3}}; \\ \sigma_2 &= \sqrt{-\rho^{\frac{1}{3}} \left\{\cos\tfrac{\phi}{3} + \sqrt{3}\sin\tfrac{\phi}{3}\right\} - \tfrac{k_1}{3}}; \\ \sigma_3 &= \sqrt{-\rho^{\frac{1}{3}} \left\{\cos\tfrac{\phi}{3} - \sqrt{3}\sin\tfrac{\phi}{3}\right\} - \tfrac{k_1}{3}}. \end{aligned} \tag{7}$$

ρ and ϕ are calculated as

$$\rho = \sqrt{-q^3}, \tag{8}$$

$$x = \rho^2 - r^2, \tag{9}$$

$$\phi = \tan^{-1}\left(\frac{\sqrt{x}}{r}\right). \tag{10}$$

The parameters q and r are given by the equations

$$q = \frac{1}{3}k_2 - \frac{1}{9}k_1^2 \quad ; \; r = \frac{1}{6}\left(k_1k_2 - 3k_3\right) - \frac{1}{27}k_1^3. \tag{11}$$

The coefficients k_1, k_2, and k_3 are determined as a function of matrix elements (μ_{ij}; $\forall i = 1,2,3$; $\forall j = 1,2,3$)

$$\begin{aligned} k_1 &= -\left(\mu_{11} + \mu_{22} + \mu_{33}\right), \\ k_2 &= \mu_{11}\mu_{22} + \mu_{11}\mu_{33} + \mu_{22}\mu_{33} - \left(\mu_{12}^2 + \mu_{13}^2 + \mu_{23}^2\right), \\ k_3 &= \mu_{12}^2\mu_{33} + \mu_{13}^2\mu_{22} + \mu_{23}^2\mu_{11} - \mu_{11}\mu_{22}\mu_{33} - 2\mu_{12}\mu_{13}\mu_{23}. \end{aligned} \tag{12}$$

since

$$\begin{array}{ll} \mu_{11} = \frac{1}{N}\sum_{i=1}^{N} U_i^2 - \left(\overline{U}\right)^2; & \mu_{12} = \frac{1}{N}\sum_{i=1}^{N} U_i V_i - \overline{U}\,\overline{V}; \\ \mu_{13} = \frac{1}{N}\sum_{i=1}^{N} U_i W_i - \overline{U}\,\overline{W}; & \mu_{22} = \frac{1}{N}\sum_{i=1}^{N} V_i^2 - \left(\overline{V}\right)^2; \\ \mu_{23} = \frac{1}{N}\sum_{i=1}^{N} V_i W_i - \overline{V}\,\overline{W}; & \mu_{33} = \frac{1}{N}\sum_{i=1}^{N} W_i^2 - \left(\overline{W}\right)^2. \end{array} \tag{13}$$

The direction cosines $(l_j, m_j, n_j;\ \forall j = 1,2,3)$ for the eigenvalue problem (λ_j), matrix elements (μ_{ij}), and velocities' dispersion (σ_j) [i.e., $\lambda_j = \sigma_j^2$; $\forall j = 1,2,3$] where $(\lambda_1 > \lambda_2 > \lambda_3)$, along three axes (Elsanhoury et al., 2015), are mathematically given as follows:

$$l_j = \left[\mu_{22}\mu_{33} - \sigma_i^2\left(\mu_{22} + \mu_{33} - \sigma_i^2\right) - \mu_{23}^2\right]/D_j, \tag{14}$$

$$m_j = \left[\mu_{23}\mu_{13} - \mu_{12}\mu_{33} + \sigma_j^2\mu_{12}\right]/D_j, \tag{15}$$

$$n_j = \left[\mu_{12}\mu_{23} - \mu_{13}\mu_{22} + \sigma_j^2\mu_{13}\right]/D_j, \tag{16}$$

and

$$\begin{gathered} D_j^2 = \left(\mu_{22}\mu_{33} - \mu_{23}^2\right)^2 + \left(\mu_{23}\mu_{13} - \mu_{12}\mu_{33}\right)^2 \\ + \left(\mu_{12}\mu_{23} - \mu_{13}\mu_{22}\right)^2 + 2[\left(\mu_{22} + \mu_{33}\right)\left(\mu_{23}^2 - \mu_{22}\mu_{33}\right) \\ + \mu_{12}\left(\mu_{23}\mu_{13} - \mu_{12}\mu_{33}\right) + \mu_{13}\left(\mu_{12}\mu_{23} - \mu_{13}\mu_{22}\right)]\sigma_j^2 \\ + \left(\mu_{33}^2 + 4\mu_{22}\mu_{33} + \mu_{22}^2 - 2\mu_{23}^2 + \mu_{12}^2 + \mu_{13}^2\right)\sigma_j^4 \\ -2\left(\mu_{22} + \mu_{33}\right)\sigma_j^6 + \sigma_j^8, \end{gathered}$$

where $(l_j^2 + m_j^2 + n_j^2 = 1)$ is an initial test for our code and (l_2) is known as the vertex longitude (Mihalas et al., 1983; Elsanhoury, 2016).

3.2. Galactic longitude and latitude parameters

Let L_j and B_j, $(\forall j = 1,2,3)$ be the galactic longitude and latitude of the directions, respectively, which correspond to the extreme values of the dispersion, then

$$L_j = tan^{-1}\left(\frac{-m_j}{l_j}\right), \tag{17}$$

$$B_j = sin^{-1}\left(n_j\right). \tag{18}$$

3.3. Fundamental solar elements

For Program stars having space velocities $(\overline{U}, \overline{V}, \overline{W})$, the components of the Sun's velocities are referred to as $(U_\odot, V_\odot,$ and $W_\odot)$, where $(U_\odot = -\overline{U})$, $(V_\odot = -\overline{V})$, and $(W_\odot = -\overline{W})$. Therefore, the solar elements $(S_\odot,\ l_A,\ b_A)$ with the spatial velocity considered may take the following

$$S_\odot = \sqrt{\overline{U}^2 + \overline{V}^2 + \overline{W}^2}, \tag{19}$$

$$l_A = tan^{-1}\left(\frac{-\overline{V}}{\overline{U}}\right), \tag{20}$$

$$b_A = sin^{-1}\left(\frac{-\overline{W}}{S_\odot}\right). \tag{21}$$

In what follows, we estimate the Sun's local velocity from radial velocities, by letting $X^\bullet_\odot, Y^\bullet_\odot$ and $Z^\bullet_\odot$ be the components of the Sun's velocity relative to x, y, and z axes with the origin at the observer. Therefore, $X^\bullet_\odot = -\overline{V_x}$, $Y^\bullet_\odot = -\overline{V_y}$, and $Z^\bullet_\odot = -\overline{V_z}$. From there, we can find the apex of the Sun's trajectory from formulae

$$\alpha_A = tan^{-1}\left(\frac{Y^\bullet_\odot}{X^\bullet_\odot}\right), \tag{22}$$

$$\delta_A = tan^{-1}\left(\frac{Z^\bullet_\odot}{\sqrt{\left(X^\bullet_\odot\right)^2 + \left(Y^\bullet_\odot\right)^2}}\right), \tag{23}$$

and the Sun's velocity is given by

$$S_\odot = \sqrt{\left(X^\bullet_\odot\right)^2 + \left(Y^\bullet_\odot\right)^2 + \left(Z^\bullet_\odot\right)^2}, \tag{24}$$

where $S_\odot$ denotes the absolute value of the Sun's velocity relative to the three Program stars under consideration, (l_A, b_A) are galactic longitude and galactic latitude of the solar apex, respectively, and (α_A, δ_A) is the galactic right ascension and declination with respective manner of the solar apex. Figure 3 shows the HiVels in three projection velocities (i.e., U, V, and W) with respect to the galactic center. This allows researchers to examine stellar populations in the circumsolar area of the Galaxy. Of great interest is the UV plane, where all stars can be properly classified into multiple families. Nearby stars mostly originate from the disk, which has a distinctive velocity dispersion $\sim$ -500 km s^{-1} along each coordinate.

Following the computational algorithm developed by Elsanhoury et al. (2015) to serve and compute the VEPs and the convergent point (CP) of three HiVels Programs, including various kinematic parameters (e.g., spatial velocities, velocities dispersion, direction cosines, solar elements, ... etc.) and the ratios of (σ_2/σ_1) and (σ_3/σ_1), into which the obtained results of these ratios ranged from 0.75 to 0.86 & 0.40 to 0.60, respectively.

Stars in the galactic disk have the largest velocity dispersion in the radial direction, which is why it is said that the velocity ellipsoid's longest axis points approximately in the direction of the galactic center. The velocity ellipsoid's longest axis points roughly in the direction of the galactic center because one of its axes is oriented normally to the plane of the galaxy, allowing the other two axes to also lie there. The angle between a group of stars' average V_r vector and the line connecting the Sun to the galactic center is known as the vertex deviation or longitude of the vertex (l_2). The kinematic characteristics of the studied star population (e.g., HiVels) can be examined in this way. In the MW's thin disk, the velocity ellipsoid is oriented almost along the radial direction (toward the galactic center) because the vertex's longitude is usually near 0^o (Elsanhoury et al., 2015; Elsanhoury, 2016; Bisht et al., 2020; Mihalas & Binney, 1981). The original numerical results are listed in Table 2 and Table 3, including the solar elements.

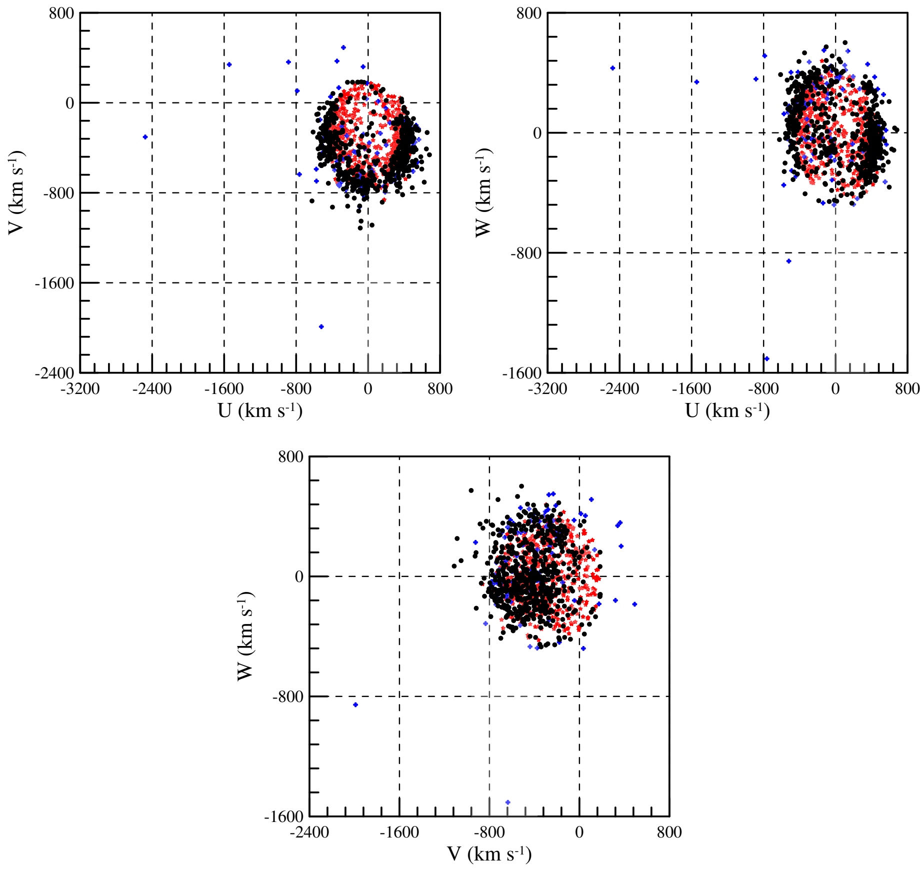

Figure 3. Velocity components distributions UV, UW, and VW relative to the Galaxy center of three Program HiVels calculated by us. Program I: black closed circles – 591 HiVels, Program II: blue closed pluses – 87 HiVels, and Program III: red open circles – 519 stars.

3.4. Convergent point (CP)

Usually, stars in a stellar association and/or moving group have a common chemical composition, space velocity, age, and distance which indicates that they are moving across the Galaxy together. The apparent movement of these stars as viewed by the observer, however, varies slightly based on their position in the MW. Their PM vectors indicate the velocity and bearing of the stars' passage across the MW. Typically, in stellar kinematics, the coherent point in the direction of one location on the celestial sphere is well-defined as a vertex, apex, or CP with equatorial coordinates (A_o, D_o). Several techniques are stated for this purpose like i) the classical CP method (Boss, 1908), ii) the individual star apex (AD-diagram), known and developed by Chupina et al. (2001, 2006), and iii) the convergent point search method (CPSM) edited by Galli et al. (2012). In the present analysis, we specifically focus on the AD chart method, which relies on the distribution of individual apexes within the equatorial coordinate system and was employed by Bisht et al. (2020); Elsanhoury (2021); Maurya et al. (2021); Elsanhoury et al. (2024). Eqs. (4), (5), and (6) of average space velocity vectors are used in this manner to get the equatorial coordinates of the (A_o, D_o) in the following formulae. The obtained results are listed in the last row of Table 2.

$$A_o = \tan^{-1}\left(\frac{\overline{V_y}}{\overline{V_x}}\right) \quad \& \quad D_o = \tan^{-1}\left(\frac{\overline{V_z}}{\sqrt{\overline{V_x^2} + \overline{V_y^2}}}\right) \tag{25}$$

4. Galactic rotation constants

The stars offer a perfect sample for understanding the composition and development of the galactic disk and determining the MW constant parameters. These constants are crucial for understanding how stars, gas, and other objects move within the Galaxy's gravitational potential. Moreover, they describe the rotation curve and the motion of objects relative to the galactic center. The differential rotation and local angular velocity (i.e., local rotational features) of the MW Galaxy are described by two fundamental parameters, A and B (i.e., Oort's constants (Oort, 1927a)). They give the dynamic structure of the MW, including its rotation curve and the distribution of matter within it. In addition to helping quantify the shear and turbulent flow of the rotation of the Galaxy, these constants are used to examine how the velocity of stars varies with their distance from the galactic center. According to Oort (Oort, 1927a,b), the constants (A & B) were then calculated using V_r and PM, yielding the values $A \approx$ 19 km s^{-1} kpc^{-1} and $B \approx$ -24 km s^{-1} kpc^{-1}. In his study, the relatively smooth rotating curve of the Galaxy was demonstrated, cutting out the hypothesis that it rotates like a rigid body.

Table 2. VEPs and CPs of the three Program HiVels calculated by us.

Parameters	Program I: 591 HiVels ($0.10 \leq d$(kpc) ≤ 15.40)
$\overline{V_x}$, $\overline{V_y}$, $\overline{V_z}$ (km s^{-1})	-218.43 ± 14.76, 139.79 ± 11.83, -343.81 ± 18.54
$\overline{U}$, $\overline{V}$, $\overline{W}$ (km s^{-1})	56.61 ± 7.52, -426.79 ± 20.66, 9.88 ± 3.14
λ_1, λ_2, λ_3 (km s^{-1})	239234, 137669, 38478.70
σ_1, σ_2, σ_3 (km s^{-1})	489.12 ± 22.12, 371.04 ± 19.26, 196.16 ± 14.01
$\overline{\sigma_o}$ (km s^{-1})	644.50 ± 15.40
$(l_1, m_1, n_1)^o$	0.2869 ± 0.002, -0.9578 ± 0.002, -0.0220 ± 0.001
$(l_2, m_2, n_2)^o$	-0.9145 ± 0.003, -0.2806 ± 0.002, 0.2916 ± 0.002
$(l_3, m_3, n_3)^o$	0.2854 ± 0.002, 0.0636 ± 0.001, 0.9563± 0.002
L_j, $j = 1, 2, 3$	73.33, 162.94, 167.45
B_j, $j = 1, 2, 3$	-1.26, 16.95, 73.00
$S_\odot$ (km s^{-1})	430.641 ± 20.75
$(l_A, b_A)^o$	82.44 ± 0.11, -1.32 ± 0.02
$(\alpha_A, \delta_A)^o$	-32.62 ± 0.17, -52.97 ± 0.86
$(A_o, D_o)^o$	147.382 ± 0.08, -52.973 ± 0.14
Parameters	Program II: 87 HiVels ($0.30 \leq d$(kpc) ≤ 108.64)
$\overline{V_x}$, $\overline{V_y}$, $\overline{V_z}$ (km s^{-1})	-256.92 ± 16.03, 276.45 ± 16.63, -232.17 ± 15.24
$\overline{U}$, $\overline{V}$, $\overline{W}$ (km s^{-1})	114.88 ± 10.72, -422.77 ± 20.56, 66.39 ± 8.15
λ_1, λ_2, λ_3 (km s^{-1})	309649, 226100, 108921
σ_1, σ_2, σ_3 (km s^{-1})	556.46 ± 23.59, 475.50 ± 21.81, 330.03 ± 18.17
$\overline{\sigma_o}$ (km s^{-1})	802.92 ± 28.34
$(l_1, m_1, n_1)^o$	0.2759 ± 0.002, 0.9610 ± 0.002, 0.0181 ± 0.001
$(l_2, m_2, n_2)^o$	-0.9528 ± 0.003, 0.2710 ± 0.002, 0.1368 ± 0.001
$(l_3, m_3, n_3)^o$	0.1265 ± 0.001, -0.0550 ± 0.001, 0.9904 ± 0.002
L_j, $j = 1, 2, 3$	-73.98, -164.13, -156.51
B_j, $j = 1, 2, 3$	1.04, 7.86, 82.07
$S_\odot$ (km s^{-1})	443.100 ± 21.05
$(l_A, b_A)^o$	-74.80 ± 0.12, -8.62 ± 0.34
$(\alpha_A, \delta_A)^o$	-47.10 ± 0.15, -31.60 ± 0.18
$(A_o, D_o)^o$	132.902 ± 0.09, -31.600 ± 0.18
Parameters	Program III: 519 HiVels ($0.29 \leq d$(kpc) ≤ 16.44)
$\overline{V_x}$, $\overline{V_y}$, $\overline{V_z}$ (km s^{-1})	-157.41 ± 12.55, 121.11 ± 11.00, -230.11 ± 15.17
$\overline{U}$, $\overline{V}$, $\overline{W}$ (km s^{-1})	14.46 ± 3.80, -303.43 ± 17.42, 10.98 ± 3.31
λ_1, λ_2, λ_3 (km s^{-1})	143180, 80747.10, 34595.50
σ_1, σ_2, σ_3 (km s^{-1})	378.39 ± 19.45, 284.16 ± 16.86, 186.00 ± 13.64
$\overline{\sigma_o}$ (km s^{-1})	508.45 ± 22.55
$(l_1, m_1, n_1)^o$	0.1307 ± 0.001, -0.9910 ± 0.002, -0.0275 ± 0.002
$(l_2, m_2, n_2)^o$	-0.9403 ± 0.003, -0.1327 ± 0.001, 0.3134 ± 0.003
$(l_3, m_3, n_3)^o$	0.3142 ± 0.003, 0.0151 ± 0.001, 0.0950 ± 0.002
L_j, $j = 1, 2, 3$	82.49, 171.97, 177.24
B_j, $j = 1, 2, 3$	-1.57, 18.27, 71.67
$S_\odot$ (km s^{-1})	303.977 ± 17.43
$(l_A, b_A)^o$	87.27 ± 0.11, -2.07 ± 0.03
$(\alpha_A, \delta_A)^o$	-37.57 ± 0.16, -49.20 ± 0.14
$(A_o, D_o)^o$	142.43 ± 0.08, -49.21 ± 0.14

Table 3. Ratios of velocity dispersions and the solar velocities for our three program HiVels and other components of the disks by different authors.

Type	$S_{\odot}$ km s^{-1}	σ_2/σ_1	σ_3/σ_1	Ref.
Program I – 591 stars	430.641 ± 20.75	0.76	0.40	[1]
Program II – 87 stars	443.100 ± 21.05	0.86	0.60	[1]
Program III – 591 stars	303.977 ± 17.43	0.75	0.49	[1]
Inner halo ($d \leq 15$ kpc)	213.36 ± 14.61	0.70	0.52	[2]
Outer halo ($d = 15 - 20$ kpc)	210.14 ± 14.50	0.76	0.61	[2]
Halo disk	-	0.56	0.56	[3]
Thin disk	-	0.57	0.46	[3]
Thick disk	-	0.57	0.52	[3]
Thin disk	-	0.62	0.62	[4]
Thick disk	-	0.51	0.51	[4]
$8.9 \geq M_V \geq 8.0$	-	0.72 ± 0.04	0.62 ± 0.04	[5]
$M_V \geq 9.0$	-	0.67 ± 0.05	0.56 ± 0.04	[5]

[1] Current study, [2] Nouh & Elsanhoury (2020), [3] Yan et al. (2020), [4] Soubiran et al. (2003), [5] Dyer (1956).

Following this, numerous attempts have been made using different tracers to calculate the Oort constants and illustrate the galactic rotation. After reviewing the earlier data, Kerr & Lynden-Bell (1986) came to the following conclusions: $A = 14.40 \pm 1.20$ km s^{-1} kpc^{-1} and $B = -12.00 \pm 2.80$ km s^{-1} kpc^{-1}. To determine that $A = -14.82 \pm 0.84$ km s^{-1} kpc^{-1} and $B = -12.37 \pm 0.64$ km s^{-1} kpc^{-1}, Feast & Whitelock (1997) adopted 220 galactic Cepheids with Hipparcos PM. Considering $R_o = 7.66 \pm 0.32$ kpc by Metzger et al. (1998), therefore, the obtained comparable outcome for $A = 15.50 \pm 0.40$ km s^{-1} kpc^{-1} using Cepheids. Recently, Nouh & Elsanhoury (2020) obtained a comparable outcome of A & B with 15.60 ± 1.60 & -13.90 ± 1.80 km s^{-1} kpc^{-1}, Elsanhoury et al. (2021) computed Oort constants like $A = 14.69 \pm 0.61$ km s^{-1} kpc^{-1} and $B = -16.70 \pm 0.67$ km s^{-1} kpc^{-1}, and Elsanhoury (2024) has $A = 12.91 \pm 0.16$ km s^{-1} kpc^{-1} and $B = -13.16 \pm 0.27$ km s^{-1} kpc^{-1}.

Here, we calculate the Oort constants (A & B) considered for three-Program HiVels using the LAMOST and DR3 archives. With an amplitude that rises linearly with distance, we follow the discovery that the heliocentric V_r shows a double sine-wave variation with galactic longitude (Balona & Feast, 1974).

$$V_r = -2A(R_{gc} - R_o)\sin l \cos b + K, \tag{26}$$

where (K; km s^{-1}) is a correction term that can be understood as systematic motions of massive stellar groups, systematic inaccuracies in the V_r caused by motions within stellar atmospheres, gravitational redshift, and erroneous wavelength combinations (Feast & Shuttleworth, 1965), where l and b stand for the specific star's longitude and latitude, respectively, $R_o = 8.20 \pm 0.10$ kpc (Bland-Hawthorn et al., 2019) is the distance from the Sun to the galactic center, and

Table 4. Velocity dispersion and rotation constants for three program HiVels under study.

Parameters	Program I	Program II	Program III
σ_2/σ_1	0.76	0.86	0.75
A (km s^{-1} kpc^{-1})	15.427 ± 0.25	3.883 ± 0.51	16.510 ± 0.25
B (km s^{-1} kpc^{-1})	-21.095 ± 0.22	-11.029 ± 0.30	-21.227 ± 0.22
$\|A - B\|$ (km s^{-1} kpc^{-1})	36.522 ± 6.04	14.912 ± 3.86	37.737 ± 6.14
V_o (km s^{-1})	299.48 ± 17.31	122.28 ± 11.06	309.44 ± 17.59

Program I: (591 stars); $0.10 \leq d$(kpc) ≤ 15.40
Program II (87 stars; $0.30 \leq d$ (kpc) ≤ 108.64
Program III (519 stars); $0.29 \leq d$(kpc) ≤ 16.44

R_{gc} is the star's radial distance from the galactic center, the cylindrical radius vector, and it is determined by

$$R_{gc}^2 = R_o^2 + d^2 - 2R_o d \cos l. \tag{27}$$

Table 4 lists our three HiVels Investigations for which we computed the Oort constants A and B. Row 2 least-squares fit of Eq. (26) yields the first Oort constant (A; km s^{-1} kpc^{-1}), while the third row is the second Oort constant (B; km s^{-1} kpc^{-1}) calculated using the relation $(\sigma_2/\sigma_1)^2 = -B/(A-B)$ (Bisht et al., 2020). The ratio (σ_2/σ_1) is calculated using the computational method covered in Section 3. The angular velocity is shown in row 4 ($|A - B|$; km s^{-1} kpc^{-1}), and the rotational velocity V_o calculated using the well-known relation $V_o = |A - B|\, R_o$, where $R_o = 8.20 \pm 0.10$ kpc, is given in the last row. Our mean Oort and rotational constants as compared with previous researchers are presented in Table 5, it's clear that Oort constants and galactic rotational parameters were computed for about 304,267 main sequence stars from the Gaia DR1 using data at a typical heliocentric distance of 230 pc (Bovy, 2017), a sample of stars within 500 parsecs used the Gaia DR2 data (Li et al., 2019), using the trigonometric parallaxes and PMs of over 25,000 young stars from the Gaia DR2 dataset (Krisanova et al., 2020), using a sample of halo red giants and the radial and spatial velocities of 1,583 red giant stars collected from the SEGUE-1 and SEGUE-2 surveys (Nouh & Elsanhoury, 2020), a sample of 5,627 A-type stars selected from the LAMOST surveys that were located within 0.60 kpc (Wang et al., 2021), devoted mid to late M-type stars (Elsanhoury et al., 2021), for a clean sample of stars (130,665) within 100 pc (Guo & Qi, 2023) computed these constants with a maximum likelihood model by using the Gaia Catalog of Nearby Stars (GCNS) (Gaia Collaboration et al., 2021), and for high and low galactic latitudes of K dwarfs (Elsanhoury & Al-Johani, 2023).

Table 5. Velocity dispersion and rotation constants for three program HiVels under study.

A (km s^{-1} kpc^{-1})	B (km s^{-1} kpc^{-1})	$\|A-B\|$ (km s^{-1} kpc^{-1})	Methods V_r/PMs	References
11.94 ± 0.29	-17.78 ± 0.24	25.07 ± 5.01	V_r	[1]
15.30 ± 0.40	-11.90 ± 0.40	27.20	PMs	[2]
15.10 ± 0.10	-13.40 ± 0.40	28.40	PMs	[3]
15.73 ± 0.32	-12.67 ± 0.34	28.40	PMs	[4]
15.60 ± 1.60	-13.90 ± 1.80	29.50 ± 0.20	V_r	[5]
16.31 ± 0.89	-11.99 ± 0.79	28.30	PMs	[6]
14.69 ± 0.61	-16.70 ± 0.67	31.39	V_r	[7]
15.60 ± 1.60	-15.80 ± 1.70	31.40 ± 2.30	V_r	[8]
12.91 ± 0.16	-13.16 ± 0.27	26.06	V_r	[9]

[1] Current study, [2] Bovy (2017), [3] Li et al. (2019), [4] Krisanova et al. (2020), [5] Nouh & Elsanhoury (2020), [6] Wang et al. (2021), [7] Elsanhoury et al. (2021), [8] Guo & Qi (2023), [9] Elsanhoury & Al-Johani (2023).

5. Discussion and conclusion

The velocity distribution (U, V, W) of stars in three spatial directions $(\sigma_1, \sigma_2, \sigma_3)$ is known as the velocity ellipsoid in galactic kinematics. The ellipsoid's shape reflects the anisotropy in the star motion, and its primary axes relate to the directions with the largest and smallest velocity dispersion. Velocity ellipsoids vary among star populations. For instance, thick disk and halo stars exhibit more isotropic ellipsoids and bigger velocity dispersions than thin disk stars, which have comparatively small dispersions. In this study, we calculated the kinematical parameters, convergent point, and the Oort constants A and B of three Programs (i.e., 591, 87, and 519 stars) of high velocity stars located $0.10 \geq d(kpc) \geq 109$. The following summarizes the main findings of the current studies:

- We retrieved high velocities in both mean spatial velocities (U, V, W, and V_{space}; km s^{-1}), Program I (56.61 ± 7.52, -426.79 ± 20.66, 9.88 ± 3.14, and 430.641 ± 20.75), Program II (114.88 ± 10.72, -422.77 ± 20.56, 66.39 ± 8.15, and 443.100 ± 21.05), and Program III (14.46 ± 3.80, -303.43 ± 17.42, 10.98 ± 3.31, an 303.977 ± 17.43) and the mean velocity dispersion (σ_1, σ_2, σ_3, and σ_o; km s^{-1}), Program I (489.12 ± 22.12, 371.04 ± 19.26, 196.16 ± 14.01, and 644.50 ± 15.40), Program II (556.46 ± 23.59, 475.50 ± 21.81, 330.03 ± 18.17, and 802.92 ± 28.34), and Program III (378.39 ± 19.45, 284.16 ± 16.86, 186.00 ± 13.64, and 508.45 ± 22.55).
- Our obtained results of the l_2 are: -0^o.9145 ± 0^o.003 (Program I), -0^o.9528 ± 0^o.003 (Program II), and -0.9403 ± 0^o.003 (Program III), these obtained results are in line with that of Mihalas & Binney (1981) and many authors, e.g., $l_2 = -0°.3454$, $-0°.6735$, and $-0°.0264$ (Elsanhoury, 2024) and $-0^o.87$ & $-0^o.91$ (Elsanhoury et al., 2018).

• We have determined the convergent points (A_o, D_o), Program I: $147^o.382 \pm 0^o.08$, $-52^o.973 \pm 0^o.14$, Program II: $132^o.902 \pm 0^o.09$, $-31^o.600 \pm 0^o.18$, and Program III: $142^o.43 \pm 0^o.08$, $-49^o.21 \pm 0^o.14$.

• The mean values of Oort's constants are $A = 11.94 \pm 0.29$ and $B = -17.78 \pm 0.24$ km s^{-1} kpc^{-1} as listed in Table 5. Therefore, the mean angular velocity $|A - B| = 25.07 \pm 5.01$ km s^{-1} kpc^{-1} and the rotational velocity $V_o = 243.72 \pm 15.61$ km s^{-1}.

• In regions where stars are to be expected to be quite a way distant on average like our consideration of HiVels, the measured values of A and B may contain significant inaccuracies due to both long distances (Lewis, 1990) and the choice of kinematic model (V_r or PM) (Hanson, 1987) as Table 4 makes it clear with Program II. Lewis (1990) reported that this is due to two effects. First, the proper motion along declination μ_δ nearly equal to the ratio of (V_y/d), i.e., $\mu_\delta \sim (V_y/d)$ and $A \sim \mu_\delta$, thus if d increases, the value of A will decrease, as clearly seen in Program II of Table 4. But V_y is also dependent on $(\cos\alpha)$ and on distance d (see Eq. 5). Therefore, these two effects should affect both A and B in a roughly equal manner (Lewis, 1990).

Acknowledgements. We sincerely thank the anonymous referee for their valuable suggestions, which have significantly improved the quality of this paper. This work presents results from the European Space Agency space mission Gaia. Gaia data are being processed by the Gaia Data Processing and Analysis Consortium (DPAC). Funding for the DPAC is provided by national institutions, in particular, the institutions participating in the Gaia MultiLateral Agreement (MLA). The Gaia mission website is https://www.cosmos.esa.int/gaia. The Gaia archive website is https://archives.esac.esa.int/gaia.

The Guoshoujing Telescope (Large Sky Area Multi-Object Fiber Spectroscopic Telescope LAMOST) is a National Major Scientific Project built by the Chinese Academy of Sciences. Funding for the project has been provided by the National Development and Reform Commission. LAMOST is operated and managed by the National Astronomical Observatories, Chinese Academy of Sciences. The author extend their appreciation to the Deanship of Scientific Research at Northern Border University, Arar, KSA for funding this research work through the project number "NBU-FFR-2025-237-03".

Data availability: We have used the different data sets for high velocity stars, which are publicly available at the following links:

- https://vizier.cds.unistra.fr/viz-bin/VizieR?-source=J/ApJS/252/3
- https://vizier.cds.unistra.fr/viz-bin/VizieR?-source=J/AJ/166/12
- https://vizier.cds.unistra.fr/viz-bin/VizieR?-source=J/AJ/167/76
- https://vizier.cds.unistra.fr/viz-bin/VizieR-3?-source=I/355/gaiadr3&-out.max=50&-out.form=HTML%20Table&-out.add=_r&-out.add=_RAJ,_DEJ&-sort=_r&-oc.form=sexa

References

Abadi, M. G., Navarro, J. F., & Steinmetz, M., An Alternative Origin for Hypervelocity Stars. 2009, *Astrophysical Journal, Letters*, **691**, L63, DOI:10.1088/0004-637X/691/2/L63

Alam, S., Albareti, F. D., Allende Prieto, C., et al., The Eleventh and Twelfth Data Releases of the Sloan Digital Sky Survey: Final Data from SDSS-III. 2015, *Astrophysical Journal, Supplement*, **219**, 12, DOI:10.1088/0067-0049/219/1/12

Balona, L. A. & Feast, M. W., A new determination from OB stars of the galactic rotation constants and the distance to the galactic centre. 1974, *Monthly Notices of the RAS*, **167**, 621, DOI:10.1093/mnras/167.3.621

Bauer, E. B., White, C. J., & Bildsten, L., Remnants of Subdwarf Helium Donor Stars Ejected from Close Binaries with Thermonuclear Supernovae. 2019, *Astrophysical Journal*, **887**, 68, DOI:10.3847/1538-4357/ab4ea4

Bisht, D., Elsanhoury, W. H., Zhu, Q., et al., An Investigation of Poorly Studied Open Cluster NGC 4337 Using Multicolor Photometric and Gaia DR2 Astrometric Data. 2020, *Astronomical Journal*, **160**, 119, DOI:10.3847/1538-3881/ab9ffd

Blaauw, A., On the origin of the O- and B-type stars with high velocities (the "runaway" stars), and some related problems. 1961, *Bulletin Astronomical Institute of the Netherlands*, **15**, 265

Bland-Hawthorn, J., Sharma, S., Tepper-Garcia, T., et al., The GALAH survey and Gaia DR2: dissecting the stellar disc's phase space by age, action, chemistry, and location. 2019, *Monthly Notices of the RAS*, **486**, 1167, DOI:10.1093/mnras/stz217

Boss, L. J., Convergent of a moving cluster in Taurus. 1908, *Astronomical Journal*, **26**, 31, DOI:10.1086/103802

Bovy, J., Galactic rotation in Gaia DR1. 2017, *Monthly Notices of the RAS*, **468**, L63, DOI:10.1093/mnrasl/slx027

Bovy, J., Allende Prieto, C., Beers, T. C., et al., The Milky Way's Circular-velocity Curve between 4 and 14 kpc from APOGEE data. 2012, *Astrophysical Journal*, **759**, 131, DOI:10.1088/0004-637X/759/2/131

Bromley, B. C., Kenyon, S. J., Geller, M. J., et al., Hypervelocity Stars: Predicting the Spectrum of Ejection Velocities. 2006, *Astrophysical Journal*, **653**, 1194, DOI:10.1086/508419

Buder, S., Sharma, S., Kos, J., et al., The GALAH+ survey: Third data release. 2021, *Monthly Notices of the RAS*, **506**, 150, DOI:10.1093/mnras/stab1242

Capuzzo-Dolcetta, R. & Fragione, G., High-velocity stars from close interaction of a globular cluster and a supermassive black hole. 2015, *Monthly Notices of the RAS*, **454**, 2677, DOI:10.1093/mnras/stv2123

Chupina, N. V., Reva, V. G., & Vereshchagin, S. V., The geometry of stellar motions in the nucleus region of the Ursa Major kinematic group. 2001, *Astronomy and Astrophysics*, **371**, 115, DOI:10.1051/0004-6361:20010337

Chupina, N. V., Reva, V. G., & Vereshchagin, S. V., Kinematic structure of the corona of the Ursa Major flow found using proper motions and radial velocities of single stars. 2006, *Astronomy and Astrophysics*, **451**, 909, DOI:10.1051/0004-6361:20054009

Contigiani, O., Rossi, E. M., & Marchetti, T., On measuring the Galactic dark matter halo with hypervelocity stars. 2019, *Monthly Notices of the RAS*, **487**, 4025, DOI:10.1093/mnras/stz1547

Cui, X.-Q., Zhao, Y.-H., Chu, Y.-Q., et al., The Large Sky Area Multi-Object Fiber Spectroscopic Telescope (LAMOST). 2012, *Research in Astronomy and Astrophysics*, **12**, 1197, DOI:10.1088/1674-4527/12/9/003

De Silva, G. M., Freeman, K. C., Bland-Hawthorn, J., et al., The GALAH survey: scientific motivation. 2015, *Monthly Notices of the RAS*, **449**, 2604, DOI:10.1093/mnras/stv327

Dyer, Jr., E. R., An analysis of the space motions of red dwarf stars. 1956, *Astronomical Journal*, **61**, 228, DOI:10.1086/107332

Eilers, A.-C., Hogg, D. W., Rix, H.-W., & Ness, M. K., The Circular Velocity Curve of the Milky Way from 5 to 25 kpc. 2019, *Astrophysical Journal*, **871**, 120, DOI:10.3847/1538-4357/aaf648

Elsanhoury, W. H., Kinematics and Velocity Ellipsoid Parameters of Stellar Groups and Open Star Clusters: II Cool Stars. 2016, *Astrophysics*, **59**, 246, DOI:10.1007/s10511-016-9430-0

Elsanhoury, W. H., Photometric and kinematical analysis of Koposov 12 and Koposov 43 open clusters. 2021, *Journal of Astrophysics and Astronomy*, **42**, 90, DOI:10.1007/s12036-021-09771-x

Elsanhoury, W. H., Kinematical and ellipsoidal properties of the inner-halo hot subdwarfs observed in Gaia DR3 and LAMOST DR7. 2024, *New Astronomy*, **112**, 102258, DOI:10.1016/j.newast.2024.102258

Elsanhoury, W. H., A, H. A., Elkholy, E. A., & Çınar, D. C., Deeply Comprehensive Astrometric, Photometric, and Kinematic Studies of the Three OCSN Open Clusters with Gaia DR3. 2024, *arXiv e-prints*, arXiv:2412.07871, DOI:10.48550/arXiv.2412.07871

Elsanhoury, W. H. & Al-Johani, A. S., Kinematical and ellipsoidal properties of K dwarfs in the solar neighborhood of the Gaia era. 2023, *Astronomische Nachrichten*, **344**, e20230047, DOI:10.1002/asna.20230047

Elsanhoury, W. H., Nouh, M. I., & Abdel-Rahman, H. I., Kinematics and Velocity Ellipsoid of the Solar Neighborhood White Dwarfs. 2015, *Revista Mexicana de Astronomia y Astrofisica*, **51**, 199, DOI:10.48550/arXiv.1503.03595

Elsanhoury, W. H., Nouh, M. I., Branham, R. L., & Al-Johani, A. S., Kinematics and ellipsoidal motion of the mid to late M-type stars. 2021, *Astronomische Nachrichten*, **342**, 989, DOI:10.1002/asna.20210019

Elsanhoury, W. H., Postnikova, E. S., Chupina, N. V., et al., The Pleiades apex and its kinematical structure. 2018, *Astrophysics and Space Science*, **363**, 58, DOI:10.1007/s10509-018-3268-3

Feast, M. & Whitelock, P., Galactic kinematics of Cepheids from HIPPARCOS proper motions. 1997, *Monthly Notices of the RAS*, **291**, 683, DOI:10.1093/mnras/291.4.683

Feast, M. W. & Shuttleworth, M., The kinematics of B stars, cepheids, galactic clusters and interstellar gas in the Galaxy. 1965, *Monthly Notices of the RAS*, **130**, 243, DOI:10.1093/mnras/130.4.245

Feltzing, S., Zhao, G., Walton, N. A., & Whitelock, P., eds. 2014, IAU Symposium, Vol. **298**, *Setting the scene for Gaia and LAMOST*

Gaia Collaboration, Prusti, T., de Bruijne, J. H. J., et al., The Gaia mission. 2016, *Astronomy and Astrophysics*, **595**, A1, DOI:10.1051/0004-6361/201629272

Gaia Collaboration, Smart, R. L., Sarro, L. M., et al., Gaia Early Data Release 3. The Gaia Catalogue of Nearby Stars. 2021, *Astronomy and Astrophysics*, **649**, A6, DOI:10.1051/0004-6361/202039498

Gaia Collaboration, Vallenari, A., Brown, A. G. A., et al., Gaia Data Release 3. Summary of the content and survey properties. 2023, *Astronomy and Astrophysics*, **674**, A1, DOI:10.1051/0004-6361/202243940

Galli, P. A. B., Teixeira, R., Ducourant, C., Bertout, C., & Benevides-Soares, P., A new method for calculating the convergent point of a moving group. 2012, *Astronomy and Astrophysics*, **538**, A23, DOI:10.1051/0004-6361/201118277

Gnedin, O. Y., Gould, A., Miralda-Escudé, J., & Zentner, A. R., Probing the Shape of the Galactic Halo with Hypervelocity Stars. 2005, *Astrophysical Journal*, **634**, 344, DOI:10.1086/496958

Guo, S. & Qi, Z., Oort Constants and Local Stellar Kinematics from GCNS. 2023, *Universe*, **9**, 252, DOI:10.3390/universe9060252

Gvaramadze, V. V., Gualandris, A., & Portegies Zwart, S., On the origin of high-velocity runaway stars. 2009, *Monthly Notices of the RAS*, **396**, 570, DOI:10.1111/j.1365-2966.2009.14809.x

Hanson, R. B., Lick Northern Proper Motion Program. II. Solar Motion and Galactic Rotation. 1987, *Astronomical Journal*, **94**, 409, DOI:10.1086/114481

Hills, J. G., Hyper-velocity and tidal stars from binaries disrupted by a massive Galactic black hole. 1988, *Nature*, **331**, 687, DOI:10.1038/331687a0

Huang, Y., Liu, X. W., Yuan, H. B., et al., The Milky Way's rotation curve out to 100 kpc and its constraint on the Galactic mass distribution. 2016, *Monthly Notices of the RAS*, **463**, 2623, DOI:10.1093/mnras/stw2096

Justham, S., Wolf, C., Podsiadlowski, P., & Han, Z., Type Ia supernovae and the formation of single low-mass white dwarfs. 2009, *Astronomy and Astrophysics*, **493**, 1081, DOI:10.1051/0004-6361:200810106

Kenyon, S. J., Bromley, B. C., Geller, M. J., & Brown, W. R., Hypervelocity Stars: From the Galactic Center to the Halo. 2008, *Astrophysical Journal*, **680**, 312, DOI:10.1086/587738

Kerr, F. J. & Lynden-Bell, D., Review of galactic constants. 1986, *Monthly Notices of the RAS*, **221**, 1023, DOI:10.1093/mnras/221.4.1023

Krisanova, O. I., Bobylev, V. V., & Bajkova, A. T., Galactic Rotation Parameters Based on Stars from Active Star-Forming Regions with Data from the Gaia DR2 Catalogue. 2020, *Astronomy Letters*, **46**, 370, DOI:10.1134/S1063773720060067

Kunder, A., Kordopatis, G., Steinmetz, M., et al., The Radial Velocity Experiment (RAVE): Fifth Data Release. 2017, *Astronomical Journal*, **153**, 75, DOI:10.3847/1538-3881/153/2/75

Lei, Z., Zhao, J., Németh, P., & Zhao, G., Hot Subdwarf Stars Identified in Gaia DR2 with Spectra of LAMOST DR6 and DR7. I. Single-lined Spectra. 2020, *Astrophysical Journal*, **889**, 117, DOI:10.3847/1538-4357/ab660a

Leonard, P. J. T., The Maximum Possible Velocity of Dynamically Ejected Runaway Stars. 1991, *Astronomical Journal*, **101**, 562, DOI:10.1086/115704

Leonard, P. J. T. & Duncan, M. J., Runaway Stars from Young Star Clusters Containing Initial Binaries. II. A Mass Spectrum and a Binary Energy Spectrum. 1990, *Astronomical Journal*, **99**, 608, DOI:10.1086/115354

Lewis, J. R., Faint stars and Oort's constants. 1990, *Monthly Notices of the RAS*, **244**, 247

Li, C., Zhao, G., & Yang, C., Galactic Rotation and the Oort Constants in the Solar Vicinity. 2019, *Astrophysical Journal*, **872**, 205, DOI:10.3847/1538-4357/ab0104

Li, Q.-Z., Huang, Y., Dong, X.-B., et al., On the Origins of Extreme Velocity Stars as Revealed by Large-scale Galactic Surveys. 2023, *Astronomical Journal*, **166**, 12, DOI:10.3847/1538-3881/acd1dc

Li, Y.-B., Luo, A. L., Lu, Y.-J., et al., 591 High-velocity Stars in the Galactic Halo Selected from LAMOST DR7 and Gaia DR2. 2021, *Astrophysical Journal, Supplement*, **252**, 3, DOI:10.3847/1538-4365/abc16e

Liao, J., Du, C., Deng, M., et al., The Origin of High-velocity Stars Considering the Impact of the Large Magellanic Cloud. 2024, *Astronomical Journal*, **167**, 76, DOI:10.3847/1538-3881/ad18c4

Liu, J. C., Zhu, Z., & Hu, B., Constructing a Galactic coordinate system based on near-infrared and radio catalogs. 2011, *Astronomy and Astrophysics*, **536**, A102, DOI:10.1051/0004-6361/201116947

Luo, A. L., Zhang, H.-T., Zhao, Y.-H., et al., Data release of the LAMOST pilot survey. 2012, *Research in Astronomy and Astrophysics*, **12**, 1243, DOI:10.1088/1674-4527/12/9/004

Majewski, S. R., Schiavon, R. P., Frinchaboy, P. M., et al., The Apache Point Observatory Galactic Evolution Experiment (APOGEE). 2017, *Astronomical Journal*, **154**, 94, DOI:10.3847/1538-3881/aa784d

Marchetti, T., Rossi, E. M., & Brown, A. G. A., Gaia DR2 in 6D: searching for the fastest stars in the Galaxy. 2019, *Monthly Notices of the RAS*, **490**, 157, DOI:10.1093/mnras/sty2592

Maurya, J., Joshi, Y. C., Elsanhoury, W. H., & Sharma, S., Photometric and Kinematic Study of the Open Clusters SAI 44 and SAI 45. 2021, *Astronomical Journal*, **162**, 64, DOI:10.3847/1538-3881/ac0138

Metzger, M. R., Caldwell, J. A. R., & Schechter, P. L., The Shape and Scale of Galactic Rotation from Cepheid Kinematics. 1998, *Astronomical Journal*, **115**, 635, DOI:10.1086/300198

Mihalas, D. & Binney, J. 1981, *Galactic astronomy. Structure and kinematics*

Mihalas, D., Binney, J., & Antonov, V. A., Book-Review - Galactic Astronomy - Structure and Kinematics. 1983, *Astrofizika*, **19**, 505

Neunteufel, P., Exploring velocity limits in the thermonuclear supernova ejection scenario for hypervelocity stars and the origin of US 708. 2020, *Astronomy and Astrophysics*, **641**, A52, DOI:10.1051/0004-6361/202037792

Nouh, M. I. & Elsanhoury, W. H., Kinematics and Velocity Ellipsoid of Halo Red Giants. 2020, *Astrophysics*, **63**, 179, DOI:10.1007/s10511-020-09624-5

O'Leary, R. M. & Loeb, A., Production of hypervelocity stars through encounters with stellar-mass black holes in the Galactic Centre. 2008, *Monthly Notices of the RAS*, **383**, 86, DOI:10.1111/j.1365-2966.2007.12531.x

Oort, J. H., Additional notes concerning the rotation of the galactic system. 1927a, *Bulletin Astronomical Institute of the Netherlands*, **4**, 91

Oort, J. H., Observational evidence confirming Lindblad's hypothesis of a rotation of the galactic system. 1927b, *Bulletin Astronomical Institute of the Netherlands*, **3**, 275

Pakmor, R., Kromer, M., Taubenberger, S., & Springel, V., Helium-ignited Violent Mergers as a Unified Model for Normal and Rapidly Declining Type Ia Supernovae. 2013, *Astrophysical Journal, Letters*, **770**, L8, DOI:10.1088/2041-8205/770/1/L8

Piffl, T., Williams, M., & Steinmetz, M., Kinematics in galactic tidal tails. A source of hypervelocity stars? 2011, *Astronomy and Astrophysics*, **535**, A70, DOI:10.1051/0004-6361/201117474

Portegies Zwart, S. F., The Characteristics of High-Velocity O and B Stars Which Are Ejected from Supernovae in Binary Systems. 2000, *Astrophysical Journal*, **544**, 437, DOI:10.1086/317190

Poveda, A., Ruiz, J., & Allen, C., Run-away Stars as the Result of the Gravitational Collapse of Proto-stellar Clusters. 1967, *Boletin de los Observatorios Tonantzintla y Tacubaya*, **4**, 86

Rockosi, C. M., Lee, Y. S., Morrison, H. L., et al., SEGUE-2: Old Milky Way Stars Near and Far. 2022, *Astrophysical Journal, Supplement*, **259**, 60, DOI:10.3847/1538-4365/ac5323

Rossi, E. M., Marchetti, T., Cacciato, M., Kuiack, M., & Sari, R., Joint constraints on the Galactic dark matter halo and Galactic Centre from hypervelocity stars. 2017, *Monthly Notices of the RAS*, **467**, 1844, DOI:10.1093/mnras/stx098

Shen, K. J., Boubert, D., Gänsicke, B. T., et al., Three Hypervelocity White Dwarfs in Gaia DR2: Evidence for Dynamically Driven Double-degenerate Double-detonation Type Ia Supernovae. 2018, *Astrophysical Journal*, **865**, 15, DOI:10.3847/1538-4357/aad55b

Soubiran, C., Bienaymé, O., & Siebert, A., Vertical distribution of Galactic disk stars. I. Kinematics and metallicity. 2003, *Astronomy and Astrophysics*, **398**, 141, DOI:10.1051/0004-6361:20021615

Steinmetz, M., Guiglion, G., McMillan, P. J., et al., The Sixth Data Release of the Radial Velocity Experiment (RAVE). II. Stellar Atmospheric Parameters, Chemical Abundances, and Distances. 2020, *Astronomical Journal*, **160**, 83, DOI:10.3847/1538-3881/ab9ab8

Taylor, M. B., TOPCAT & STIL: Starlink Table/VOTable Processing Software. 2005, in Astronomical Society of the Pacific Conference Series, Vol. **347**, *Astronomical Data Analysis Software and Systems XIV*, ed. P. Shopbell, M. Britton, & R. Ebert, 29

Wang, B. & Han, Z., Companion stars of type Ia supernovae and hypervelocity stars. 2009, *Astronomy and Astrophysics*, **508**, L27, DOI:10.1051/0004-6361/200913326

Wang, C., Huang, Y., Yuan, H., et al., The Value-added Catalog for LAMOST DR8 Low-resolution Spectra. 2022, *Astrophysical Journal, Supplement*, **259**, 51, DOI:10.3847/1538-4365/ac4df7

Wang, F., Zhang, H. W., Huang, Y., et al., Local stellar kinematics and Oort constants from the LAMOST A-type stars. 2021, *Monthly Notices of the RAS*, **504**, 199, DOI:10.1093/mnras/stab848

Xue, X. X., Rix, H. W., Zhao, G., et al., The Milky Way's Circular Velocity Curve to 60 kpc and an Estimate of the Dark Matter Halo Mass from the Kinematics of ~2400 SDSS Blue Horizontal-Branch Stars. 2008, *Astrophysical Journal*, **684**, 1143, DOI:10.1086/589500

Yan, Y., Du, C., Li, H., et al., Existence of the Metal-rich Stellar Halo and High-velocity Thick Disk in the Galaxy. 2020, *Astrophysical Journal*, **903**, 131, DOI:10.3847/1538-4357/abbd3d

Yanny, B., Rockosi, C., Newberg, H. J., et al., SEGUE: A Spectroscopic Survey of 240,000 Stars with g = 14-20. 2009, *Astronomical Journal*, **137**, 4377, DOI:10.1088/0004-6256/137/5/4377

Yu, Q. & Madau, P., Kinematics of hypervelocity stars in the triaxial halo of the Milky Way. 2007, *Monthly Notices of the RAS*, **379**, 1293, DOI:10.1111/j.1365-2966.2007.12034.x

Yu, Q. & Tremaine, S., Ejection of Hypervelocity Stars by the (Binary) Black Hole in the Galactic Center. 2003, *Astrophysical Journal*, **599**, 1129, DOI:10.1086/379546

Zhao, G., Zhao, Y.-H., Chu, Y.-Q., Jing, Y.-P., & Deng, L.-C., LAMOST spectral survey — An overview. 2012, *Research in Astronomy and Astrophysics*, **12**, 723, DOI:10.1088/1674-4527/12/7/002

Zubovas, K., Wynn, G. A., & Gualandris, A., Supernovae in the Central Parsec: A Mechanism for Producing Spatially Anisotropic Hypervelocity Stars. 2013, *Astrophysical Journal*, **771**, 118, DOI:10.1088/0004-637X/771/2/118

Contrib. Astron. Obs. Skalnaté Pleso **55/1**, 60 – 68, (2025)
https://doi.org/10.31577/caosp.2025.55.1.60

Ultraviolet photometry and reddening estimation of 105 galactic open clusters

T. Ramezani[1], **E. Paunzen**[1], **A. Gorodilov**[1] **and O.I. Pintado**[2]

[1] *Department of Theoretical Physics and Astrophysics, Masaryk University, Kotlářská 2, 611 37 Brno, Czechia (E-mail: epaunzen@physics.muni.cz)*

[2] *Consejo Nacional de Investigaciones Científicas y Técnicas, Argentina*

Received: March 23, 2025; Accepted: March 31, 2025

Abstract. This paper focuses on observing unstudied Galactic open clusters in the Ultraviolet (UV) wavelength range and analyzing their photometric data. The Gaia Data Release 3 (DR3) enables us to precisely study known Galactic open clusters. We conducted observations using the 1.54-meter Danish Telescope (DK1.54) in Chile and the 2.15-meter telescope at the Complejo Astronómico El Leoncito (CASLEO) in Argentina, employing UV filters. Furthermore, we have collected available photometric and astrometric data for our observed clusters. We aim to estimate the reddening of Galactic open clusters using UV photometry. We applied isochrone fitting to determine the reddening of the clusters using well-known members. As a final result, we present the reddening values of 105 Galactic open clusters in the UV, as determined by our photometry.

Key words: open clusters – Gaia – ultraviolet – photometry

1. Introduction

Star clusters, particularly open clusters, serve as essential laboratories for understanding stellar formation, evolution, and dynamics. Since stars within a cluster share a common origin, distance, and age, their study provides crucial insight into the broader processes of stellar evolution (Krause et al., 2020). By analyzing star clusters, we can refine our models of stellar formation and lifecycles, such as those governed by mass, composition, and environment. Studying these clusters in the Ultraviolet (UV) wavelengths is particularly important because UV observations are sensitive to young, hot, and massive stars (Hillier, 2020). These stars emit most of their light in the UV, making this wavelength regime critical for understanding the early stages of stellar evolution and the Interstellar Medium (ISM). One of the key challenges in studying star clusters is interstellar reddening (absorption or extinction; Pandey et al., 2003). This effect is caused by dust grains in the ISM that scatter and absorb starlight, causing the light from stars to shift toward redder wavelengths (Cardelli et al., 1989).

The amount of reddening is a function of the dust column density and the object's location within the Galaxy. Correcting for this reddening is essential for accurately determining stellar properties such as temperature and luminosity. Extinction models, such as the Fitzpatrick (1999) model, are commonly used to correct for these effects. These models help to remove the distortion introduced by the ISM and allow us to recover the intrinsic colours and magnitudes of stars.

Unfortunately, recent UV observations of star clusters are very scarce. Only a few Well-studied ones are also analysed in the UV (Sindhu et al., 2018). The Ultra Violet Imaging Telescope (UVIT) consortium presented some results for well-known star clusters (Jadhav et al., 2021).

In this paper, we present the status of our project to observe Galactic open clusters to study their extinction characteristics using our own observed Johnson U and archival Gaia BP, RP, and G photometry.

2. Target selection and observations

For the first case study of our project, we selected 105 southern star clusters from the list of Hunt & Reffert (2023) which are not too extended on the sky. This catalogue contains the parameters (age, reddening, and distance) and positional information of 7 167 star clusters, including moving groups, with over 700 newly discovered high-confidence clusters. They used the widely applied Hierarchical Density-Based Spatial Clustering of Applications with Noise (HDBSCAN) algorithm (McInnes et al., 2017).

We conducted observations using the 1.54-meter Danish Telescope (DK1.54) in Chile and the 2.15-meter telescope at the Complejo Astronómico El Leoncito (CASLEO) in Argentina, employing UV filters.

The DK1.54 was equipped with the Danish Faint Object Spectrograph and Camera (DFOSC) using a 2k × 2k thinned Loral CCD chip with a field of view (FOV) of 12×12 arc minutes. The 2.15-meter Jorge Sahade reflector at CASLEO was using a 2k × 2k Roper Scientific Versarray 2048B camera with a FOV of about nine arc minutes.

The exposure time for each cluster is 300 seconds, with at least two observations for each cluster.

3. Data reduction

The basic CCD reductions (bias-subtraction, dark correction, and flat-fielding) were performed with standard IRAF v2.17 routines. We removed cosmic rays whenever needed before calculating the Point Spread Function (PSF) and the instrumental magnitude for all stars.

As the next step, we matched the observed fields using the Atlas of Large-Area Digital Image Navigation (Aladin). For this, we used the IRAF task "xy2sky" to transform pixel coordinates (x, y) into the celestial coordinates (RA, DEC). After a rotation of 270 degrees, we could compare them with external catalogues.

For our purposes, we used the Gaia DR3 (Babusiaux et al., 2023) and its photometry (BP, RP, and G magnitudes) for the matching process. This was done by a newly developed pipeline software[1] based on the Match Program[2], which uses the FOCAS algorithm (Valdes et al., 1995). The script takes the Gaia data and our objects in .CSV format as input data. Loading confirmed cluster members representing main sequence stars into the script is also possible. We used Hunt & Reffert (2023) catalogue, which is based on Gaia DR3 data, to define members. We then filtered the matched stars for cluster members.

Instrumental magnitudes are typically uncalibrated values from the instrument, which depend on the specific setup (filters, detectors, and exposure times). The Gaia DR3 provides flux-calibrated low-resolution spectrophotometry (BP/RP spectra) for about 200 million sources in the wavelength range from 330 to 1050 nm (Gaia Collaboration et al., 2023). From these spectra, synthetic photometry can be derived for any passband. Existing observations can be reproduced within a few per cent over a wide range of magnitudes and colour for wide and medium bands, such as Johnson U, and with up to millimag accuracy when synthetic photometry is standardised for external sources. We first checked the available standard U photometry using The General Catalogue of Photometric Data[3]. No offsets or systematics were detected.

As the last step, we transformed our instrumental magnitudes to standard ones as described by Bessell (2005).

4. Estimating the reddening values

We generated colour-colour diagrams from Colour-Magnitude Diagrams (CMDs), including U photometry and fitted the filtered stars to find their extinction in each colour from the main sequence standard line for the different colour combinations. The standard lines are taken from the Padova database of stellar evolutionary tracks and isochrones (Bressan et al., 2012).

Fitting is done manually, using a GUI interface that allows the standard main sequence to be shifted along two axes corresponding to the combination of colours selected. The script calculates the errors for a confidence interval of 99.73%. A tutorial on the use of pipelines is available in the README.md file.

We get the reddening from U in the independent colour-colour diagram of age, distance, and metallicity. We estimate the reddening for all our observed clusters in different passbands.

[1] https://github.com/PoruchikRzhevsky/Match-pipeline
[2] http://spiff.rit.edu/match/
[3] https://gcpd.physics.muni.cz/

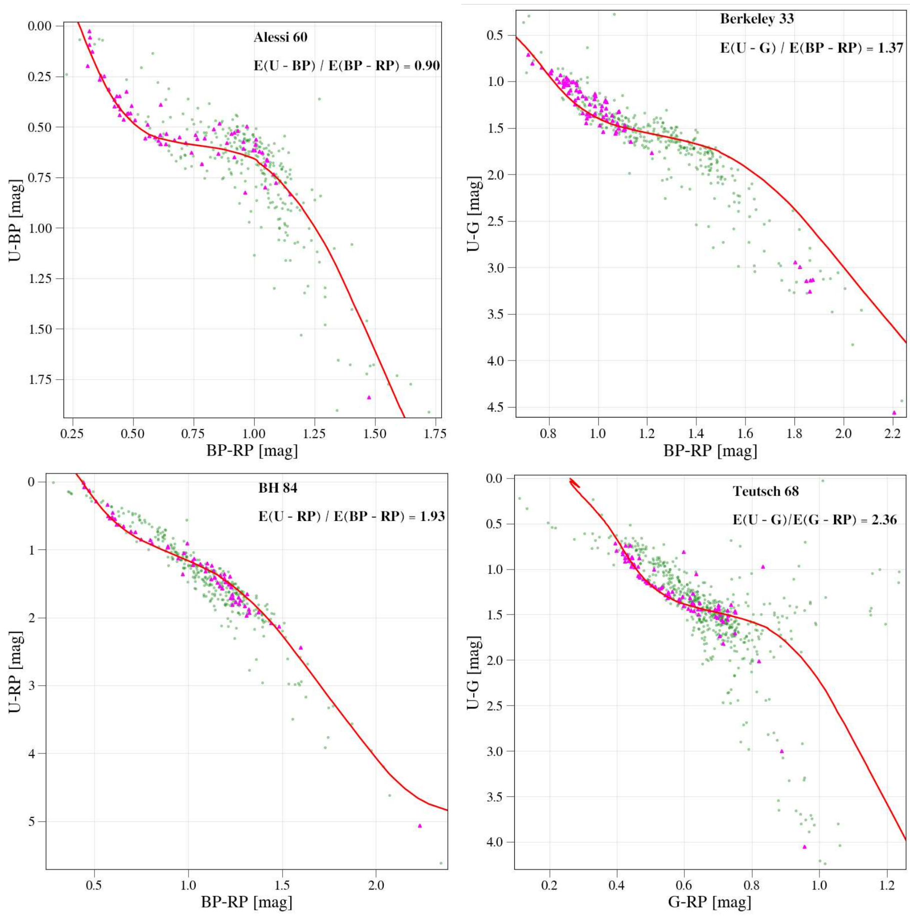

Figure 1. Colour−Colour diagrams of different clusters and filter combinations. The standard lines are taken from Bressan et al. (2012). The green dots are matched non-members and pink triangles are members from Hunt & Reffert (2023).

Figure 1 shows the Colour−Colour diagrams of different clusters and filter combinations. The green dots are matched non-members, and the pink triangles are members from Hunt & Reffert (2023).

In Table 1, we present the name of the clusters, their coordinates in RA and DEC, different extinction ratios, uncertainties of each extinction's ratios, mean value of extinctions, the distance and log age from the Hunt & Reffert (2023) catalogue. Only cluster BH 140 does not have log age in their catalogue. In its complete form, this table is only available at the CDS or upon request.

Table 1. Coordinates, reddening values, and uncertainties of clusters. In its complete form, this table is only available at the CDS or upon request. The first page is printed here for guidance regarding its form and content. The columns denote: (1) Clusters' name. (2) Right ascension (J2000; Gaia DR3). (3) Declination (J2000; GaiaDR3). (4) $E(U-BP)/E(BP-RP)$. (5) $E(U-G)/E(BP-RP)$. (6) $E(U-RP)/E(BP-RP)$. (7) $E(U-G)/E(G-RP)$. (8) $E(U-G)/E(BP-G)$. (9) Uncertainty of $E(U-BP)/E(BP-RP)$. (10) Uncertainty of $E(U-G)/E(BP-RP)$. (11) Uncertainty of $E(U-RP)/E(BP-RP)$. (12) Uncertainty of $E(U-G)/E(G-RP)$. (13) Uncertainty of $E(U-G)/E(BP-G)$. (14) Mean extinction. (15) Distance (kpc). (16) $\log t$.

(1)	(2)	(3)	(4)	(5)	(6)	(7)	(8)	(9)	(10)	(11)	(12)	(13)	(14)	(15)	(16)
Alessi_17	113.853	-15.092	1.08	1.36	2.01	2.08	3.78	0.28	0.11	0.17	0.76	0.41	2.06	3.92	8.38
Alessi_60	105.615	-1.120	0.90	1.29	1.90	2.03	2.09	0.14	0.09	0.08	0.22	0.20	1.64	2.64	8.68
Berkeley_33	104.454	-13.226	0.98	1.37	1.98	2.24	3.45	0.08	0.10	0.08	0.29	0.16	2.00	4.73	8.68
BH_72	142.843	-53.041	1.30	1.68	2.30	2.18	2.98	0.55	0.56	0.57	0.80	0.88	2.09	4.51	8.23
BH_84	150.334	-58.217	0.92	1.33	1.93	2.21	3.22	0.12	0.13	0.13	0.34	0.35	1.92	3.80	8.21
BH_87	151.162	-55.377	1.13	1.54	2.13	2.52	3.71	0.11	0.10	0.08	0.21	0.27	2.21	2.18	8.15
BH_111	167.317	-63.830	0.91	1.30	1.91	2.15	3.32	0.23	0.24	0.22	0.51	0.53	1.92	2.46	8.43
BH_132	186.725	-64.065	0.85	1.32	1.85	1.93	3.45	0.31	0.32	0.32	0.46	0.32	1.88	2.47	7.98
BH_140	193.454	-67.182	1.16	1.55	2.17	2.84	3.44	0.06	0.07	0.07	0.38	0.39	2.23	4.60	
CWNU_95	223.299	-54.108	0.59	1.00	1.63	1.63	2.60	0.18	0.17	0.18	0.68	0.74	1.49	1.05	7.37
CWNU_1733	114.240	-26.321	0.39	0.89	1.45	1.51	2.11	0.27	0.32	0.28	0.71	0.80	1.27	1.73	8.30
Czernik_29	112.095	-15.399	1.08	1.41	2.08	2.44	3.66	0.09	0.10	0.07	0.32	0.21	2.13	3.51	8.39

5. Analysis

Let us recall that stars in galaxies are born in molecular clouds (MCs). The gravitational collapse of the dense regions in the ISM of galaxies is an important mechanism to form star clusters (Keilmann et al., 2024). Dust is made up of heavy elements resulting from star nuclear burning. Dust grains are formed by reprocessing these heavy elements in the interstellar medium after they are expelled from stars by winds and explosions (Draine, 2003).

Dust (and gas) significantly affects light propagation, scattering, and absorbing photons from UV to infrared wavelengths, leading to extinction and reddening effects in astronomical observations (Schlafly & Finkbeiner, 2011). There are two different effects of extinction: 1) From the molecular cloud that the star cluster is born from; 2) From the ISM between the observer and star cluster.

Dust is not symmetrically distributed throughout space because of supernova explosions, stellar winds, magnetic fields, and star formation variations. Another complication is the composition of the ISM, which directly affects the reddening law, i.e. the variation of extinction with wavelength. Therefore, the reddening law and the amount of extinction depend on the line of sight. It is well known that the Galactic disk has regions with an extinction as high as five magnitudes

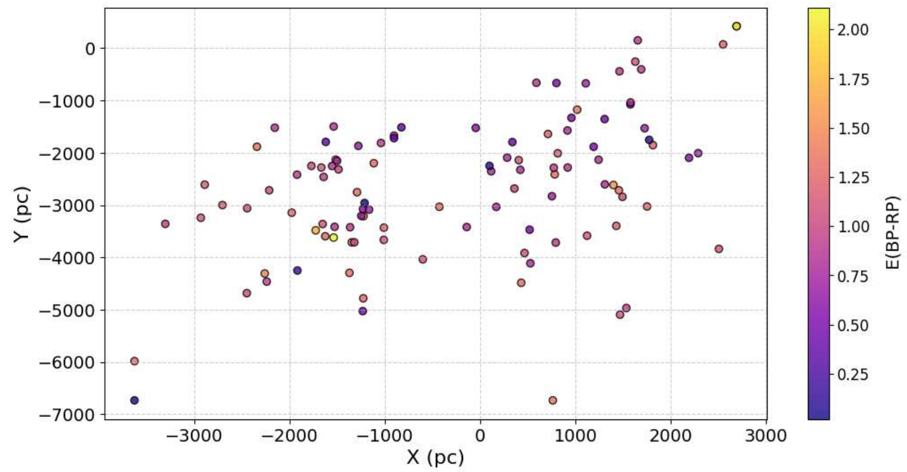

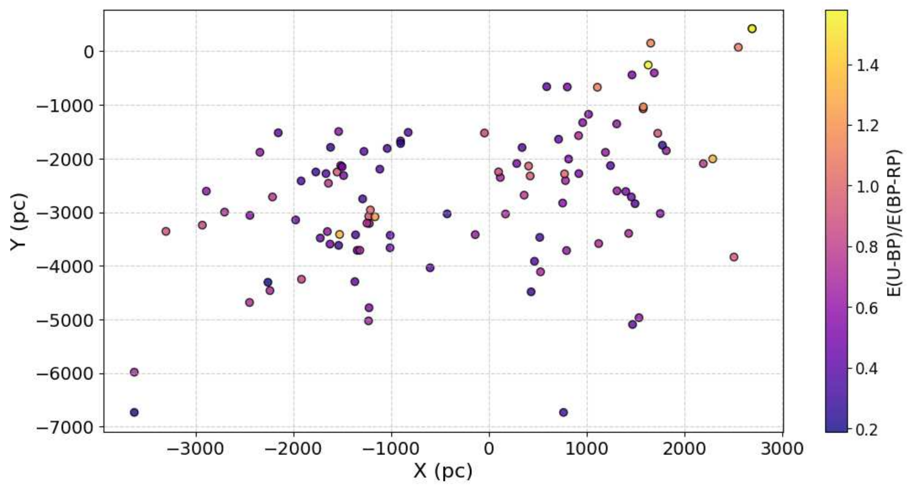

Figure 2. The upper panel shows the extinction in $(BP-RP)$. The lower panel shows the reddening ratio $E(U-BP)/E(BP-RP)$ for the 105 observed clusters in the [X, Y] coordinate system around the Sun at [0, 0], respectively.

per kpc (Neckel & Klare, 1980).

Expressing the extinction law is not unique in the literature; it has been common practice to use the ratios of two colours, for example, $E(U-B)/E(B-V)$. Using $A(V)$ as the reference extinction in the visual is arbitrary (Cardelli et al., 1989).

In Fig. 2, we present the results of our extinction estimation in [X, Y] coordinates. The X coordinate is in the direction of the Galactic centre, whereas Y is in the direction of the disk rotation. The Sun is located at [0, 0], respectively. Because all studied star clusters are located in the Galactic disk, we do not consider the third coordinate [Z] for our analysis.

With very few exceptions, the extinction is increasing for more distant clusters (Fig. 2, upper panel). This is what the current models predict, and it lends confidence in our fitting procedure.

The distribution of the reddening ratio (Fig. 2, lower panel) shows exciting features. For example, there is a continuous transition in the direction [–3000, –3000], some sudden changes on small scales [–1000, –3000], and no changes in certain lines of sight. It proves the capability to trace the ISM with extinction estimates of star clusters.

6. Conclusions and outlook

It is well known that photometric observations in the UV region help to describe the extinction law and the total absorption. Unfortunately, because of the inefficiency of modern CCD detectors, such observations are not very common any more. On the other hand, the number of star clusters is constantly increasing, caused by the excellent astrometric data of the Gaia satellite mission.

Here, we present our first case study using the synergy of ground-based UV observations and Gaia BP, RP, and G photometry to analyse star clusters. High-precision PSF photometry using published membership probabilities and a matching routine resulted in a unique data set of mainly unstudied open clusters.

Fitting standard main sequences, which are independent of age, metallicity and distance, allowed us to get absorption values and reddening laws toward 105 open clusters. Detailed maps show that our current models could be proven and have the potential to study the characteristics of the ISM in more detail.

As the next step, we plan to observe more Galactic open clusters and generate a reddening law map of the visible regions around the Sun. Another approach we will follow is the synthetic Gaia flux-calibrated low-resolution spectrophotometry (BP/RP spectra), which allows for a synthesis of photometry.

Acknowledgements. This work was supported by the grants GAČR 23-07605S, MUNI/A/1077/2022, and MUNI/A/1419/2023. We want to thank doc. RNDr. M. Zejda, Ph.D., RNDr. J. Janík, Ph.D. from the Department of Theoretical Physics and Astrophysics, Masaryk University, Brno, Czechia, and Waldemar Ogloza from Pedagogical University of Cracow, Poland, for helping us with observations.

References

Babusiaux, C., Fabricius, C., Khanna, S., et al., Gaia Data Release 3. Catalogue validation. 2023, *Astronomy and Astrophysics*, **674**, A32, DOI:10.1051/0004-6361/202243790

Bessell, M. S., Standard Photometric Systems. 2005, *Annual Review of Astron and Astrophys*, **43**, 293, DOI:10.1146/annurev.astro.41.082801.100251

Bressan, A., Marigo, P., Girardi, L., et al., PARSEC: stellar tracks and isochrones with the PAdova and TRieste Stellar Evolution Code. 2012, *Monthly Notices of the Royal Astronomical Society*, **427**, 127, DOI:10.1111/j.1365-2966.2012.21948.x

Cardelli, J. A., Clayton, G. C., & Mathis, J. S., The Relationship between Infrared, Optical, and Ultraviolet Extinction. 1989, *Astrophysical Journal*, **345**, 245, DOI:10.1086/167900

Draine, B. T., Interstellar Dust Grains. 2003, *Annual Review of Astron and Astrophys*, **41**, 241, DOI:10.1146/annurev.astro.41.011802.094840

Fitzpatrick, E. L., Correcting for the Effects of Interstellar Extinction. 1999, *Publications of the ASP*, **111**, 63, DOI:10.1086/316293

Gaia Collaboration, Montegriffo, P., Bellazzini, M., et al., Gaia Data Release 3. The Galaxy in your preferred colours: Synthetic photometry from Gaia low-resolution spectra. 2023, *Astronomy and Astrophysics*, **674**, A33, DOI:10.1051/0004-6361/202243709

Hillier, D. J., UV Spectroscopy of Massive Stars. 2020, *Galaxies*, **8**, DOI:10.3390/galaxies8030060

Hunt, E. L. & Reffert, S., Improving the open cluster census. II. An all-sky cluster catalogue with Gaia DR3. 2023, *Astronomy and Astrophysics*, **673**, A114, DOI:10.1051/0004-6361/202346285

Jadhav, V. V., Pennock, C. M., Subramaniam, A., Sagar, R., & Nayak, P. K., UOCS - III. UVIT catalogue of open clusters with machine learning-based membership using Gaia EDR3 astrometry. 2021, *Monthly Notices of the RAS*, **503**, 236, DOI:10.1093/mnras/stab213

Keilmann, E., Kabanovic, S., Schneider, N., et al., Molecular cloud matching in CO and dust in M33: II. Physical properties of giant molecular clouds. 2024, *Astronomy and Astrophysics*, **692**, A226, DOI:10.1051/0004-6361/202451451

Krause, M. G. H., Offner, S. S. R., Charbonnel, C., et al., The Physics of Star Cluster Formation and Evolution. 2020, *Space Science Reviews*, **216**, 64, DOI:10.1007/s11214-020-00689-4

McInnes, L., Healy, J., & Astels, S., hdbscan: Hierarchical density based clustering. 2017, *The Journal of Open Source Software*, **2**, DOI:10.21105/joss.00205

Neckel, T. & Klare, G., The spatial distribution of the interstellar extinction. 1980, *Astronomy and Astrophysics, Supplement*, **42**, 251

Pandey, A. K., Upadhyay, K., Nakada, Y., & Ogura, K., Interstellar extinction in the open clusters towards galactic longitude around 130^{deg}. 2003, *Astronomy and Astrophysics*, **397**, 191, DOI:10.1051/0004-6361:20021509

Schlafly, E. F. & Finkbeiner, D. P., Measuring Reddening with Sloan Digital Sky Survey Stellar Spectra and Recalibrating SFD. 2011, *Astrophysical Journal*, **737**, 103, DOI:10.1088/0004-637X/737/2/103

Sindhu, N., Subramaniam, A., & Radha, C. A., Ultraviolet stellar population of the old open cluster M67 (NGC 2682). 2018, *Monthly Notices of the RAS*, **481**, 226, DOI:10.1093/mnras/sty2283

Valdes, F. G., Campusano, L. E., Velasquez, J. D., & Stetson, P. B., FOCAS Automatic Catalog Matching Algorithms. 1995, *Publications of the ASP*, **107**, 1119, DOI:10.1086/133667

PRÁCE ASTRONOMICKÉHO OBSERVATÓRIA
NA SKALNATOM PLESE
LV, číslo 1

Zostavovateľ:	RNDr. Richard Komžík, CSc.
Vedecký redaktor:	RNDr. Augustín Skopal, DrSc.
Vydal:	Astronomický ústav SAV, Tatranská Lomnica
IČO vydavateľa:	00 166 529
Periodicita:	3-krát ročne
ISSN (on-line verzia):	1336-0337
CODEN:	CAOPF8
Rok vydania:	2025
Počet strán:	70

Contributions of the Astronomical Observatory Skalnaté Pleso are processed using
LaTeX 2_ε CAOSP DocumentClass file 3.10 ver. 2024.